Currents, Water Masses, Eddies and Jets in the Mediterranean Levantine Basin

ARTUR HECHT,* NADIA PINARDI[†] AND ALLAN R. ROBINSON

Department of Earth and Planetary Sciences, Harvard University, Cambridge, Massachusetts

ABSTRACT

Hydrographic measurements in the southeastern Levantine basin are analyzed, and the climatological water masses of the region and their seasonal variations are identified. We observe the formation of the salty and warm Levantine Surface Water layer (LSW); we characterize the subsurface Atlantic Water layer (AW); and we describe the properties of the thermocline waters, called Levantine Intermediate Waters (LIW). The baroclinic dynamical modes are computed for the climatological stratification parameters. The empirical orthogonal function (EOF) analysis of the vertical shear profiles shows that considerable energy is contained in the second EOF at the thermocline and deep levels. Maps of the baroclinic streamfunction field referred to 700 meters are displayed: 16 instantaneous flow field realizations show an intense mesoscale eddy field never revealed before in the region. The space scales of the eddies are about 100 km and a smaller scale (60–70 km) variability is also evident. The eddies are persistent, e.g., stationary for over a season, and there are periods in which only a single eddy center is present embedded in an almost quiescent flow. The velocities in the strong jets at the border of the eddies are of the order of 20–40 cm s^{-1} at the upper thermocline levels. The water mass analysis fo this eddy field shows that the AW and LIW salinity properties are distributed in filaments and patches: the maximum salinity cores of LIW are trapped in the anticyclones found in the region. An event of salinity ventilation (down to 200 m) is described that seems to involve the homogenization of the salinity properties but not convective mixing of the density structure. The traditional picture of the basin currents is compared with the mesoscale flow analyzed here, and we speculate upon possible mechanisms of water mass transport.

1. Introduction

The Mediterranean basin is divided into two major sub-basins by the shallow sill of the Strait of Sicily. The Eastern basin (Fig. 1a) can also be partitioned into two major regions, the western Ionian basin and the eastern Levantine basin. Our study is concentrated in the southeastern Levantine basin, consisting of the region between Cyprus and the coasts of the Middle East (Fig. 1b).

The whole Mediterranean is a concentration basin, i.e., evaporation exceeds precipitation and runoff (Carter 1956). The thermohaline circulation of the basin has been described by Wust (1961), and the water masses of the eastern and western basins have been characterized by Lacombe and Tchernia (1972) and Morel (1971). They consist of three distinct water mass layers: 1) a layer of Atlantic Water (AW) between the surface and approximately 100 m entering from the Strait of Gibraltar and characterized by low tempera-

tures (about 15°C) and low salinity (varying between 36.5‰ west and 38.5‰ east of Sicily); 2) a layer of Intermediate Levantine Water (LIW) between 200 and 600 m that corresponds to a subsurface salinity maximum (≥38.5‰) and is formed in the eastern Levantine basin; and finally, 3) the deep waters down to the bottom. Only AW and LIW are exchanged between the Western and Eastern basins because of the shallow sill at the Strait of Sicily. The deep waters of the Eastern and Western basins are formed separately: in the Adriatic Sea for the Eastern basin (Moskalenko and Ovchinnikov 1965) and in the Northern Balearic basin for the Western basin (Stommel 1972). The depths and the temperature–salinity characteristics of the three water mass layers vary in each subregion of the two basins due to intense air–sea interaction processes and vertical mixing with adjacent layers. One of our aims is to compute their structure in the southeastern Levantine basin.

Previous studies of the kinematics of the general circulation currents of the Mediterranean Sea are scarce, probably due to the lack of data covering the whole basin. In Fig. 2 we show the most commonly cited picture of the general circulation of the two basins (Ovchinnikov 1966). The surface currents are depicted as entering the Strait of Gibraltar, branching in the Balearic basin and Tyrrenian Sea, and flowing through the Strait of Sicily into the Eastern basin. They form a meandering current along the Libyan coast and pro-

---

* Present address: Israel Oceanographic and Limnological Research Ltd., Haifa, Israel.

† Permanent address: Istituto per lo studio delle Metodologie Geofisiche Ambientali (IMGA)-CNR, Modena, 41100 Italy.

Corresponding author address: Prof. Allan R. Robinson, Department of Earth and Planetary Sciences, Harvard University, Pierce Hall, Cambridge, MA 02138.
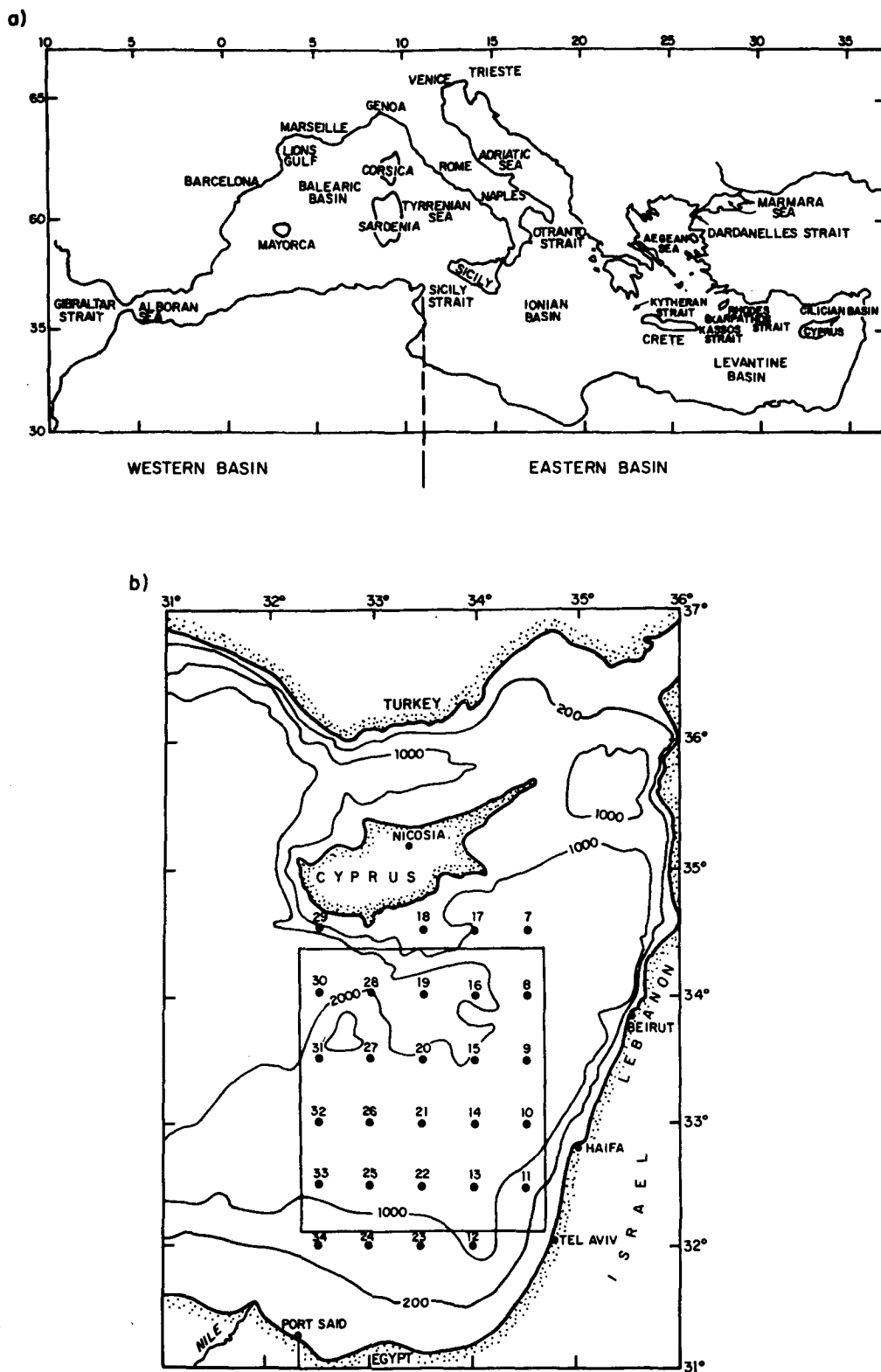
a)

WESTERN BASIN

EASTERN BASIN

b)

FIG. 1. (a) The Mediterranean basin geography and nomenclature of major sub-basin seas. (b) The topography of the southeastern Levantine basin is displayed together with the station locations indicated by a black circle and a number. A series of cruises, occupying some or all of the stations indicated, are described in the text. The rectangular box (220 × 270 km^2) indicates the domain in which the objective analysis is carried out.
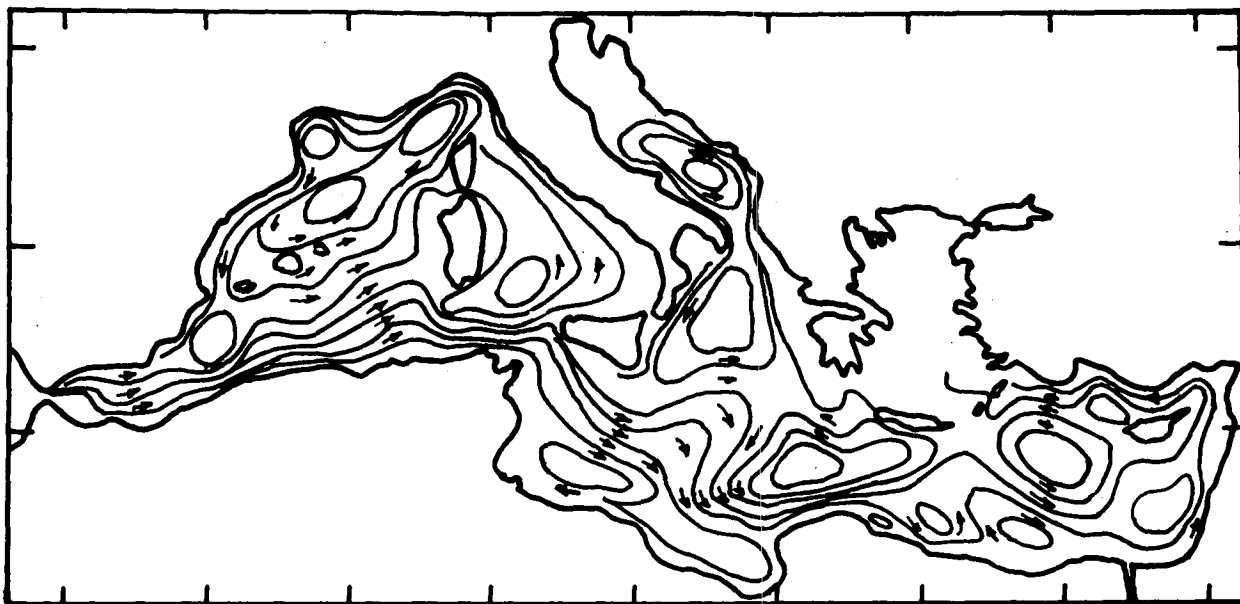
FIG. 2. Winter surface currents from dynamic height relative to 1000 m (reproduced from Ovchinnikov 1966).

gress up to the Levantine basin. Thus, the currents are generally cyclonic, forming large gyres in the Ionian Sea and southeast of Rhodes. The flow has characteristic velocities of 1–10 cm s^{-1}. At 500 m (not shown) the currents continue to be generally cyclonic, but the flow appears to be more distorted by the topography of the basin, breaking up into smaller gyres. At the Strait of Sicily the flow is reversed with respect to the surface, indicating a general outflow of LIW into the Western basin. The seasonal variations of this circulation pattern are unknown apart for a general weakening of the currents during summer. In particular, the southeastern Levantine basin emerges as an area of weak currents, branching before reaching Cyprus and continuing into the southeastern Levantine basin to form a weak cyclonic gyre. Thus, in this region, the general circulation transport is northeastward.

The thermohaline circulation of the eastern Levantine basin has been the subject of more detailed studies because of the importance of intermediate and deep water formation processes. The Rhodes gyre (Ovchinnikov 1984), the Eagean Sea (Oszoy et al. 1981), and the region offshore of Egypt (Morcos 1972) were indicated as regions of LIW formation processes, but no clear definition of the kinematics and dynamics of such events or of subsequent water spreading mechanisms is available.

A program of investigations in the Eastern Mediterranean basin, Physical Oceanography of the Eastern Mediterranean (POEM, Unesco 1984), has started an intense measurement and modeling effort to describe and interpret the circulation features of this basin. As part of the POEM effort we have analyzed a long time series of hydrographic data collected in the southeastern

Levantine by IOLR (Israel Oceanographic and Limnological Research, Ltd.). The currently available information on this region consists of some 400 deep casts (Anati 1977). Most, if not all of them, are sparse bottle casts, i.e., 10 to 20 measurements per cast, and were collected by various ships employing different methods of data acquisition and reduction. The IOLR database consists of some 500 CTD casts (that is practically continuous), carefully supervised for consistent methodology. Thus, in our opinion the inclusion of the historical database will not contribute significantly to our investigation and presentation of the climatology and instantaneous flow variability of the region. The results show an energetic mesoscale flow field with spatial scales of several tens of kilometers. The eddies appear to be stationary for more than a season and they trap waters with distinct water mass properties from the rest of the ambient water masses.

In section 2 we present the data description; in section 3 we define the climatological and seasonal water mass structure of the region; section 4 calculates empirical and dynamical modes of the vertical shear of the currents; section 5 presents the time and space scales of the mesoscale geostrophic flow field and section 6 its water mass properties. Finally, in section 7 we summarize the analysis and discuss the results.

2. Data acquisition

The present investigation is based on an analysis of the data collected during a series of 17 cruises, MC11 to MC27 (MC stands for Marine Climate), carried out in the southeastern Levantine basin by the RV *Shikmona* of the IOLR. The cruises were carried out over a period of five years, from February 1979 to August

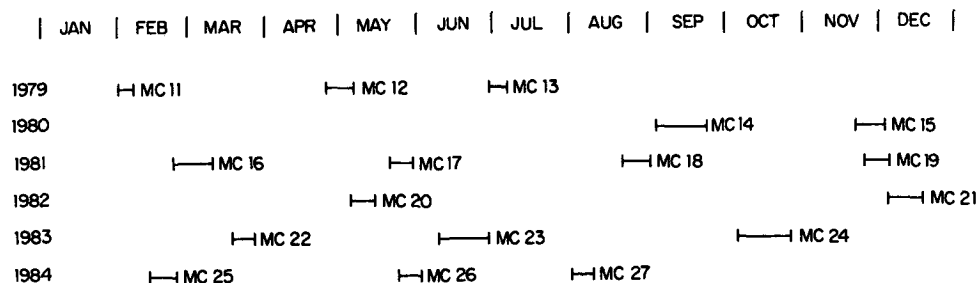| JAN | FEB | MAR | APR | MAY | JUN | JUL | AUG | SEP | OCT | NOV | DEC |

FIG. 3. Cruise schedule line.

1984 (Fig. 3 and Table 1). Each cruise lasted for about ten days and was planned so as to occupy the same grid of 28 stations situated at 0.5° intervals in a rectangular domain defined by the latitudes 32°00', 34°30'N, and longitudes 32°30', 34°30'E (Fig. 1b). The position of the vessel on station was determined by satellite navigation. During each cruise station 10 was occupied twice, once at the beginning of the cruise and again at its end. During some of the cruises additional stations were carried out or casts were repeated in order to verify some of the observed features or to acquire additional data.

The bottom topography in the domain where the MC cruises was carried out (Fig. 1b) is varied and includes some shallow regions as well as a very conspicuous feature, the Eratosthenes sea mount, which rises steeply 2000 to 800 m below sea level. The Eratosthenes sea mount is situated at 33°40'N, 32°45'E and is surrounded by stations 27, 28, 30 and 31. The measurements were carried out with a Neil Brown CTD and were calibrated against samples collected on each up-

cast at 12 predetermined levels. The samples were collected with a General Oceanics rosette and consisted of 24 samples for salinity determination (two from each bottle), as well as 12 protected and 6 unprotected thermometer temperatures. The salinity of each sample was determined with a Guildline Autosal salinometer in the shore laboratory at the end of the cruise.

Both the downcast as well as the upcast CTD measurements were recorded; however only the downcast data was subjected to further processing. This consisted of correction for the time lag of the temperature sensor (see Fofonoff et al. 1974), smoothing with a decimating average spanning ten measurements, bin-averaging around every 1 decibar, and eliminating extreme values from every bin (i.e., those measurements that exceed two standard deviations). A final validation procedure consisted of the visual examination of the T-S diagrams and the vertical temperature and salinity profiles. Moreover, the relative spread of the salinities and the temperatures for each cruise, and in particular the relative deviations of these parameters in the waters below 1000 m, were also inspected. The computations of the parameters necessary for our investigations followed the algorithms described in Fofonoff and Millard (1983). For the present investigation we used only those stations where the measurements were carried out to a depth of at least 700 m (Table 1).

3. Water masses of the region

a. Climatology

In order to describe the climatological properties of the region, the data from all the MC cruises were averaged, level by level, for each parameter. Obviously, the number of measurements available at each level diminished with depth. Thus, the database for the upper layers consisted of about 500 measurements of each parameter, while only about 360 such measurements were available at 1000 decibars and only about 50 at 2000 decibars. Even 500 measurements may not be sufficient for the computation of representative climatological parameters; thus, using the term "climatological profile" may only be defensible in the sense that data obtained during later cruises, such as the

TABLE 1. Timetable of MC (Marine Climate Program) cruises. From left to right: name of cruise, starting and ending date of cruise; number of stations at least 700 m deep; last four digits of the Julian day calendar indicating the mid-day of cruise.

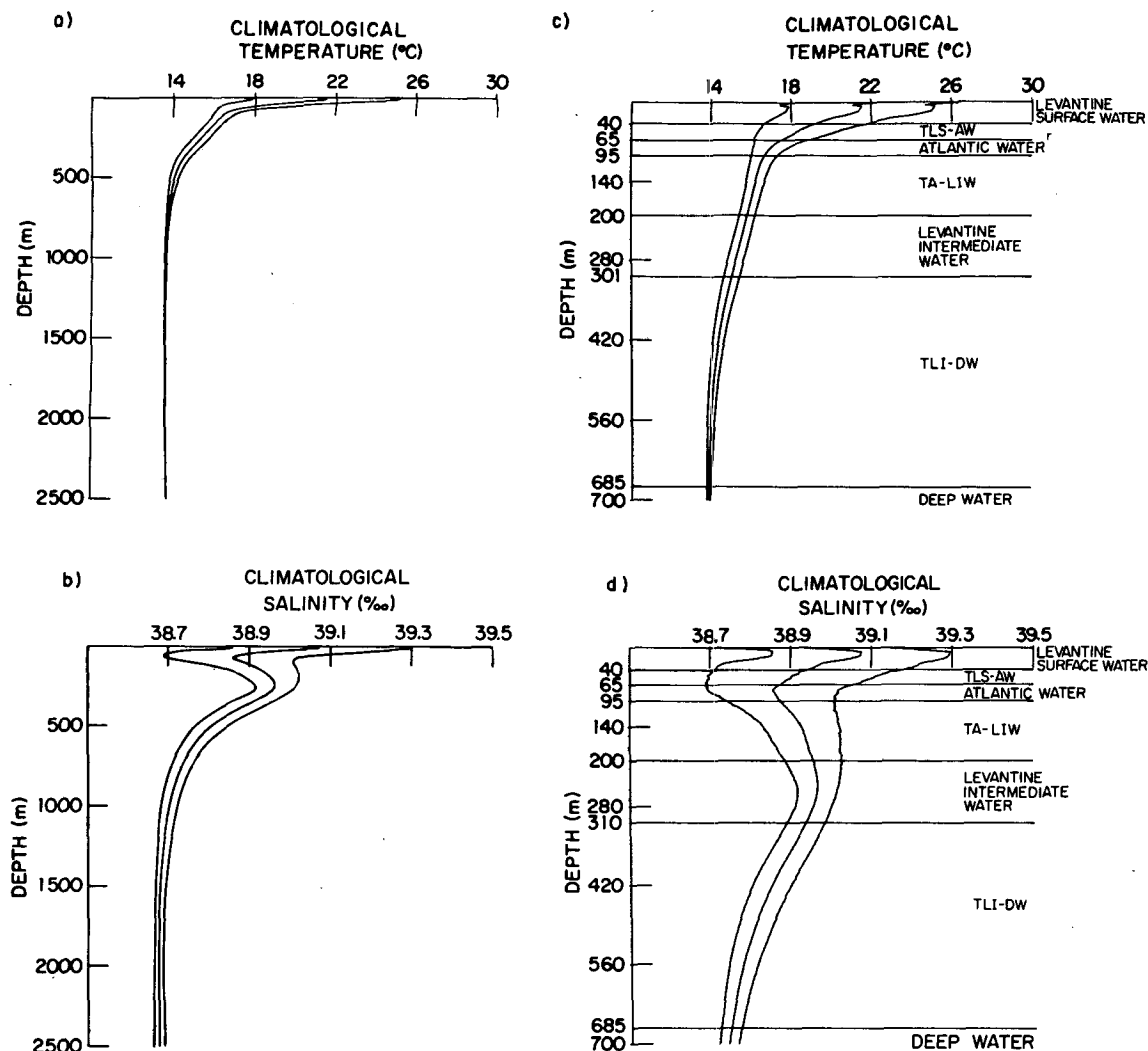| Cruise	Date	Number of stations	Mid-Julian day
MC11	01 Feb–07 Feb 1979	16	3907
MC12	25 Apr–06 May 1979	25	3993
MC13	29 Jun–06 July 1979	24	4056
MC14	02 Sep–23 Sep 1980	25	4494
MC15	20 Nov–02 Dec 1980	25	4569
MC16	22 Feb–10 Mar 1981	25	4665
MC17	20 May–29 May 1981	22	4748
MC18	20 Aug–31 Aug 1981	25	4841
MC19	24 Nov–05 Dec 1981	30	4936
MC20	04 May–14 May 1982	26	5098
MC21	03 Dec–17 Dec 1982	28	5314
MC22	17 Mar–26 Mar 1983	26	5414
MC23	08 Jun–28 Jun 1983	30	5502
MC24	05 Oct–26 Oct 1983	34	5622
MC25	12 Feb–23 Feb 1984	27	5747
MC26	22 May–31 May 1984	31	5846
MC27	30 Jul–08 Aug 1984	25	5915

FIG. 4. (a) Climatological temperature profile as a function of depth (0–2500 m). (b) Climatological salinity profile as a function of depth (0–2500 m). The ±1 standard deviation profiles are also indicated. (c) As in (a) but for depth 0–700 m. The different layers characterizing the water masses of the region are indicated by horizontal lines. Abbreviations are explained in the text. (d) As in (c) but for the salinity profile.

POEM cruises, appear to fall within the standard deviations of the "climatological profile." This term should therefore be accepted as a convenient reference relevant only in the restricted time frame of the MC cruises.

The climatological temperature and salinity profiles (Figs. 4a, b) appear to indicate that these parameters are practically constant and have almost no standard deviation from about 700 m to the bottom. Indeed, the temperature drops from 13.79 ± 0.09°C to 13.35 ± 0.01°C. These changes are very small when compared to the vertical variations that occur in other parts of the ocean (e.g., Emery and Dewar 1982; or Taft et al. 1983). Wust (1961) as well as Moskalenko and Ovchinnikov (1965) define as deep those waters with a temperature below 13.6°C and a salinity lower than

38.7‰, and place them at depths exceeding 600 m. But the southeastern Levantine basin is warmer and saltier, and such waters would only be found at depths of at least 900 m (Figs. 4a, b). Therefore one should consider defining the deep waters of the southeastern Levantine basin by higher values of temperature and salinity. In view of the vertical gradient of the temperature and the salinity profiles (Fig. 4a, b), we define the Deep Water (DW) as those waters that have a temperature of 13.8°C or lower and a salinity of 38.74‰ or lower. Such waters are found at a depth of about 700 m, which is one of our reasons for choosing 700 m as a reference level for dynamic height computations.

The expanded diagram of the climatological temperature profile (Fig. 4c) shows a steep decline in temperature in the upper few meters of water, followed by

a shallow inversion at a depth of about 10 m. The absolute difference between the extrema of this inversion is only about 0.5°C. However, the presence of this feature in the profile at a level at which we have many measurements must indicate the persistence of this phenomenon. Below the inversion, temperature drops smoothly from a maximum of 21.6° to 16.5°C at the bottom of the seasonal thermocline at about 100 m. Farther below, the temperature continues its smooth decline and reaches a value of about 14.0 ± 0.2°C at the bottom of the permanent thermocline, at about 500 m.

The expanded diagram of the climatological salinity profile (Fig. 4d) shows a steep increase in salinity from the surface to about 10 m. The climatological salinity at this level reaches a value of 39.07‰ and, taken in conjunction with the high climatological temperature at the same level, it suggests the effects of the local summer surface temperature warming and evaporation rates, which produce the Levantine Surface Water (LSW). Below this maximum the climatological salinity profile decends to a minimum of 38.86‰ at a depth of about 75 m. This minimum should be ascribed to the presence of subsurface Atlantic Water (AW) (Lacombe and Tchernia 1960). Farther below, the climatological salinity trace reaches a secondary maximum of 38.97‰ at 240 m. This maximum should correspond to the Levantine Intermediate Water (LIW) (e.g., Wust 1960). Judging from the climatological temperature profile at the appropriate levels, neither the AW nor the LIW appears to have any conspicuous temperature characteristics. In Figs. 4c, d transition regions are designated by a T prefix and the removal of the W suffix. Thus the transition region between LSW and AW is denoted by TLS-AW. This applies to all the transition regions.

The climatological T–S diagram (Fig. 5) has a characteristic S shape, which emphasizes the maximum salinity and temperature of the LSW, the minimum sa-

TABLE 2. Water mass definitions and layer depths. Salinity (S in ‰) and depth (D in meters) of the LSW, AW, LIW and DW layers for the climatological and seasonal (winter, spring, summer, autumn) averages.

		LSW	AW	LIW	DW
Climatic	S	≥ 38.95	≤ 38.87	≥ 38.94	≤ 38.74
	D	0–40	65–95	200–310	† ≥ 685
Winter	S	—	—	*38.98	
	D	—	—	75–325	† ≥ 695
Spring	S	*38.96	*38.83	*38.96	
	D	0–15	25–100	170–310	† ≥ 680
Summer	S	*39.11	*38.77	*38.98	
	D	0–25	25–105	135–315	† ≥ 690
Autumn	S	*39.24	*38.86	*38.94	
	D	0–70	80–110	230–270	† ≥ 675

* Maximum or minimum in the defined layers.
† Minimum depth at which the salinity starts to be ≤ 38.74.
N.B. The first 3 to 6 m of water are not taken into account.

linity determined by the AW, the second maximum in salinity determined by the LIW, and finally the range of low salinities of the DW. The determination of the boundaries of the layers of those water masses must take into account the seasonal distribution of the parameters and will be dealt with below. In Table 2 we indicate the layer depths and salinity values used to identify the different climatological water masses.

The squared Brunt–Väisälä frequency profile (Fig. 6) was computed from the global average of the smoothed temperature and salinity profiles. Its dominant feature is the pronounced shallow depth (40 m) maximum, which resembles similar features observed in the eastern North Atlantic Brunt–Väisälä frequency profiles (Emery et al. 1984) and is probably due to the stabilizing effect of the "fresher" AW. Below this max-
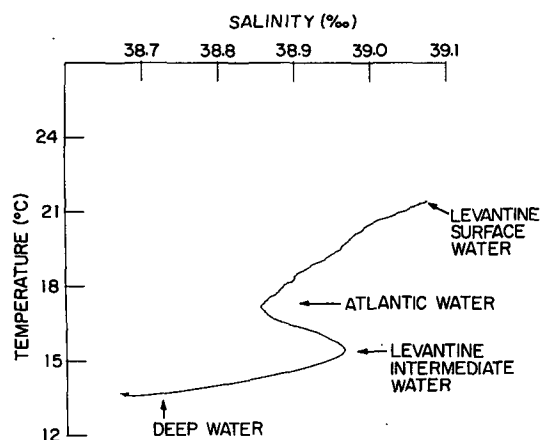

FIG. 5. Climatological T–S diagram showing the different water masses.
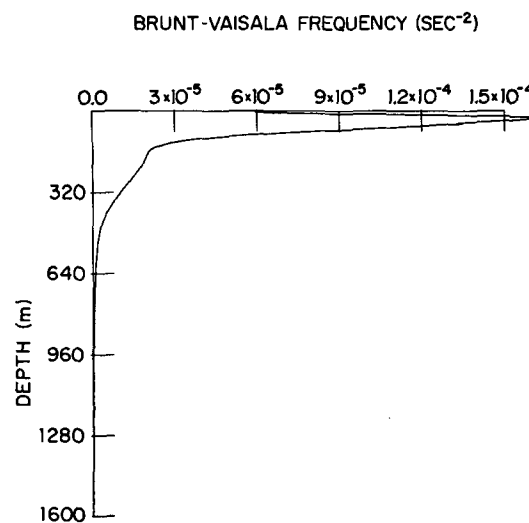

FIG. 6. Brunt–Väisälä frequency square profile, N^2, as a function of depth.

imum, the profile decreases steeply to the bottom of the seasonal thermocline (about 160 m). Eventually it reaches a depth of about 800 m where, due to the lack of temperature and salinity vertical gradients, the Brunt–Väisälä frequency becomes practically zero. The main thermocline is described by the differing gradient of the profile between 160 and 400 m; however there is no pronounced subsurface $N^2(z)$ maximum. Only a visible change in the value of the gradient appears at about 250 m. This slight inflection in the profile is probably due to LIW. A similar inflection observed in the North Atlantic Brunt–Väisälä profiles is also attributed to the Mediterranean waters that spread westward from the Strait of Gibraltar (Emery et al. 1984).

b. Seasonal characteristics

The definition of seasons in the atmosphere or in the ocean is always a controversial subject (see e.g., Trenberth 1983). In the Eastern Mediterranean Sea, Anati (1977) used all the available historical data to compute the monthly changes in heat stored in the upper 200 m of water. Assuming that seasonal changes do not penetrate below this level, he defines winter as the period of minimum heat storage and summer as the period of maximum heat storage. Essentially, Anati (1977) defines February, March and April as winter, and July, August, September and October as summer. The remaining months, May and June on the one hand, and November, December and January on the other, he defines as spring and autumn transition periods. Anati's computations preceded the MC cruises; however, the heat storage computed from the data of those cruises is in good agreement with his results (Hecht et al. 1985). Hence, we have chosen to adopt Anati's definition of the seasons in the Eastern Mediterranean Sea. For the investigation of the seasonal properties of the MC region, the cruises were grouped according to these previously defined seasons and the data within each group were averaged level by level. Obviously, the averages for each season are based on far fewer measurements than the climatological averages: we have three cruises for autumn, four for summer and winter, and six for spring. Due to this limited sample size in all the seasons, the seasonal averages should be viewed cautiously. Moreover, in bad weather, in order to prevent damage to the CTD, the measurements had to begin at a depth of a few meters. As a result, the averages in the surface layers cannot be considered representative, since more often than not, they are based on an insufficient number of measurements. Our description therefore begins at a depth of 4 to 6 m. In Table 2, the layer depths and salinity maxima are listed for every season, and we will now describe the seasonally averaged temperature and salinity profiles.

The winter average temperature of the surface layers (Fig. 7a) is about $16.6 \pm 0.6°C$. The temperatures di-

minish gently with depth and from 16.0°C (at about 170 m) coincides downwards with the climatological temperatures. The winter average salinity of the surface layers (Fig. 7b) is about $38.82 \pm 0.16‰$. The salinity increases with depth towards the LIW layer where, at about 245 m, it attains a maximum of $38.98 \pm 0.06‰$ at a temperature of $15.5 \pm 0.5°C$. The T–S diagram (Fig. 7c) clearly depicts the subsurface salinity maximum of the LIW. However, in neither the T–S diagram nor the vertical salinity profile is there any clear, unequivocal indication of the presence of the AW. This does not preclude the presence of AW in the region, as we will see in section 6. However, we cannot exclude the possibility of intense vertical mixing between the LSW and AW layers, which could homogenize the salinity properties in a unique TLS-AW/TA-LIW layer.

The spring average temperature of the surface layer (Fig. 8a) is about $21.7 \pm 2.9°C$. The surface waters have warmed considerably, and we can observe the beginning of the formation of the seasonal thermocline. The large standard deviation in the temperatures of the surface layers indicates some inhomogeneity in the warming of the region but mainly the internal variability. We will return to both subjects later in this paper. The decreasing temperatures in the deeper layers begin to coincide with the climatological temperature of 16.0°C at a depth of about 170 m, i.e., at about the same level as in the winter profile. The spring average salinity of the surface layers has also increased significantly and is about $38.96 \pm 0.15‰$ (Fig. 8b). We can observe the beginning of the formation of the seasonal halocline, but in addition to the deep maximum of the LIW, the most conspicuous feature of this profile is the salinity minimum ($38.83 \pm 0.12‰$) at about 50 m. It is misleading to interpret this enhancement of the AW signature as an indication that during the spring we have intrusion of SW into the domain. Even though the process of AW penetration in the region is present, its seasonal cycle cannot be elucidated by looking only to these average profiles. As we will see in section 6, the abundance of AW in the domain is associated with an intense mesoscale eddy field at the border and inside of which we can trace tonguelike AW intrusions in all seasons. In the spring the LIW has a maximum salinity of $38.96 \pm 0.05‰$ at about 245 m, where the temperature is $15.5 \pm 0.4°C$. Both water masses, the AW as well as the LIW, are conspicuous on the T–S diagram (Fig. 8c), where one can also note the beginning of the formation of LSW.

The summer average temperature in the surface layer (Fig. 9a) reaches its yearly peak of $25.3 \pm 2.4°C$. Nevertheless, at about the same depth as before, i.e., 175 m, temperatures have dropped to the level of the climatological values, i.e., 16.0°C. The summer-average salinity in the surface layer (Fig. 9b), $39.11 \pm 0.14‰$, is not yet at its yearly peak but is representative of the high salinities attained by the LSW (see also the T–S summer diagram in Fig. 9c). The minima of the AW
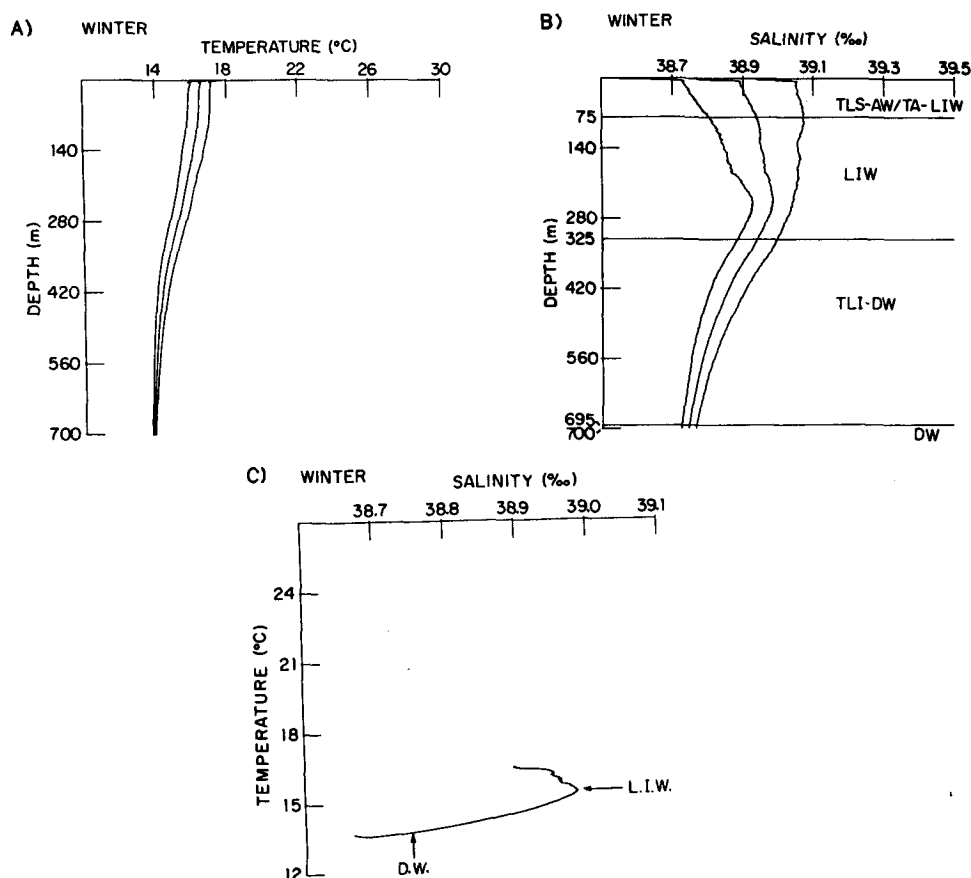
FIG. 7. Temperature (a) and salinity (b) profiles and *T-S* diagram (c) for winter cruises average.

is 38.77 ± 0.12‰ at about 50 m, and the maxima of the LIW is 38.98 ± 0.04‰ at about 245 m, where the temperature is 15.5 ± 0.3°C.

Finally, as the cooling begins, the autumn average temperature of the surface layers (Fig. 10a) drops to 20.7 ± 1.2°C while the salinity increases to 39.24 ± 0.09‰ (Fig. 10b). The upper mixed layer is well established and contains the LSW that decends down to about 40 m. As in the other seasons, the average temperatures in the autumn descend to their climatological value (16°C) at a depth of about 170 m. The minimum salinity (Fig. 10b) of the AW (38.86 ± 0.22‰) appears at about 85 m. The maximum salinity of the LIW (38.94 ± 0.02‰) appears at about 245 m, where the temperature is 15.4 ± 0.4°C (Fig. 10c).

As the AW moves from the Strait of Gibraltar to the Levantine basin, its salinity changes drastically. At the Strait of Sicily, for example, the characteristic salinity is 37.5‰ (Morel 1971), while at the Strait of Crete (Hecht 1986) as well as in the Cilician basin (Ozsoy et al. 1981) the characteristic salinity is 38.6‰. Any definition of the AW is therefore a strictly local one. In view of the climatological and seasonal salinity profiles, we define the AW as the upper layer of water whose

salinity is less than 38.87‰ (see Table 2). This layer is particularly visible in the spring and summer average profiles. We cannot exclude the possibility that its abundance during this period is associated with the presence of the LSW layer, which prevents the AW from mixing and evaporating.

As we have pointed out before, the LIW is characterized by a subsurface maximum in the salinity profile. Since this maximum does not necessarily have the same magnitude all over the basin, the LIW has been defined differently in different regions of the Mediterranean Sea (e.g., Morcos 1972; Ozturgut 1976; Ozsoy et al. 1981). In view of the climatological and seasonal salinity profiles described above, we define the LIW as the subsurface layer whose salinity is at least 38.94‰ (see Table 2). As we have seen, such a layer is present throughout the year at a depth of about 245 m (Table 2) and has a temperature of 15.5 ± 0.4°C.

As the foregoing description has indicated, in the region of the MC cruises the main seasonal changes in temperature take place only to 170 m. Below this level each of the seasonally averaged temperatures is identical with the climatological temperature (16.0 ± 0.4°C), thus supporting Anati's (1977) findings.
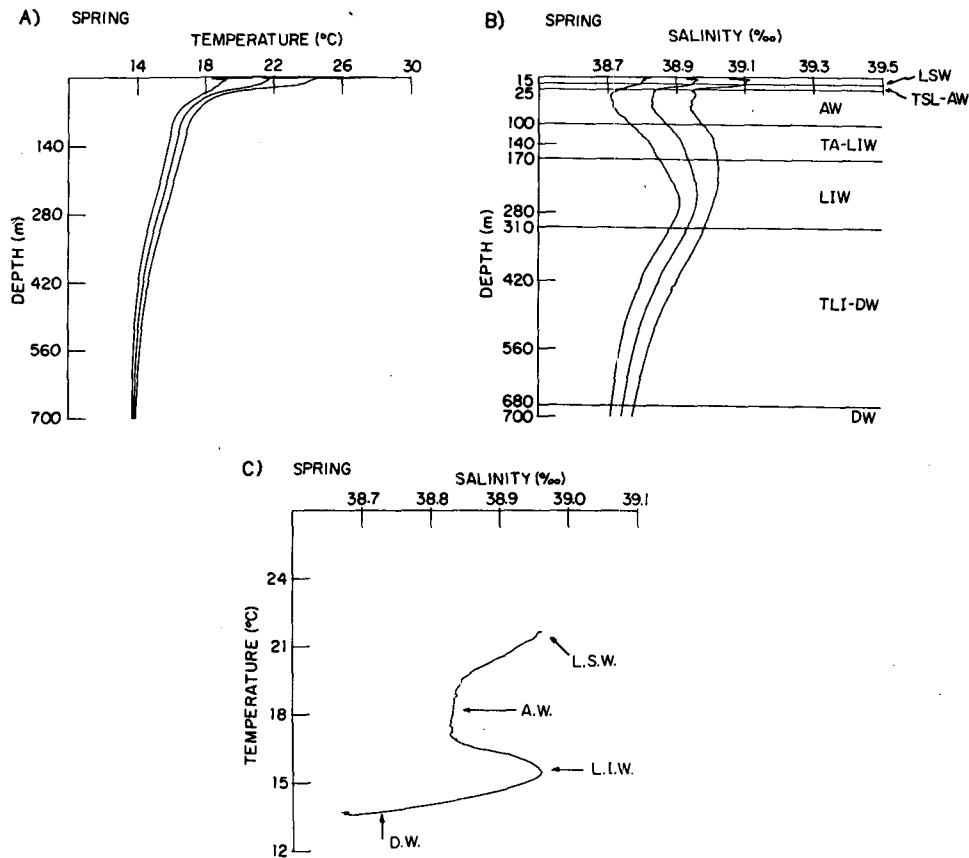
FIG. 8. As in Fig. 7 but for spring cruises average.

Taking the maximum salinity of the LIW as a reference point, the changes between winter and spring or spring and summer (from 38.98 ± 0.06‰ to 38.96 ± 0.05‰ to 38.94 ± 0.04‰, see Table 2) are within the bounds of the standard deviations of our measurements and are therefore not significant. However, the change between summer and autumn (from 38.98 ± 0.04‰ to 38.94 ± 0.02‰) could be significant, and this indicates a dilution of the LIW with waters that could come from either the AW or the DW. The parallel increase in the autumn salinity of the AW may indeed point to an exchange of water between the LIW and the AW, although this is not necessarily so, since the AW can also enhance its salinity through an exchange of water with the LSW. At the same time, the increased thickness of the TLI-DW layer in autumn indicates that mixing with the DW is active, such that the LIW reaches its lowest seasonal salinity value.

What we have here is a low salinity body of water sandwiched between two saltier layers, the upper one warmer and the lower one cooler than the fresher waters between them. At the interface between the AW and the LSW we have the classical situation that could induce double-diffusive instability (e.g., Turner 1974). A comparison between the relatively smooth winter average salinity profile (Fig. 7b), the only season in which there is no definite average AW layer, and the "jagged" average salinity profiles (Fig. 9b, 10b) exhibit irregularities between the LSW and the AW layer that closely resemble the pictures presented by Turner's (1978, see Figs. 3 and 5) experiments depicting intrusion into a density gradient. The evidence is even more dramatic when one compares particular stations, such as station 19 from MC24 of October 1983 (Fig. 11a) and the same station from MC25 of February 1984 (Fig. 11b). At the other interface, between the AW and the LIW, we have warmer fresher waters above cooler saltier waters. As far as double-diffusion instability is concerned, this is a stable environment, and therefore the mixing of fresher waters into the LIW, whether from above or below, must be implemented by other processes.

In order to gain additional insight into the annual cycle, the cruise average temperatures and salinity profiles as well as the corresponding $T-S$ diagrams and $N(z)$ profiles were arranged according to the middate of the cruise, irrespective of the year in which the cruise took place (Table 1 and Fig. 12). Thus we have at least one realization for each month except January and April. Since there is practically no seasonal variability below a depth of 500 decibars, and in order to enhance
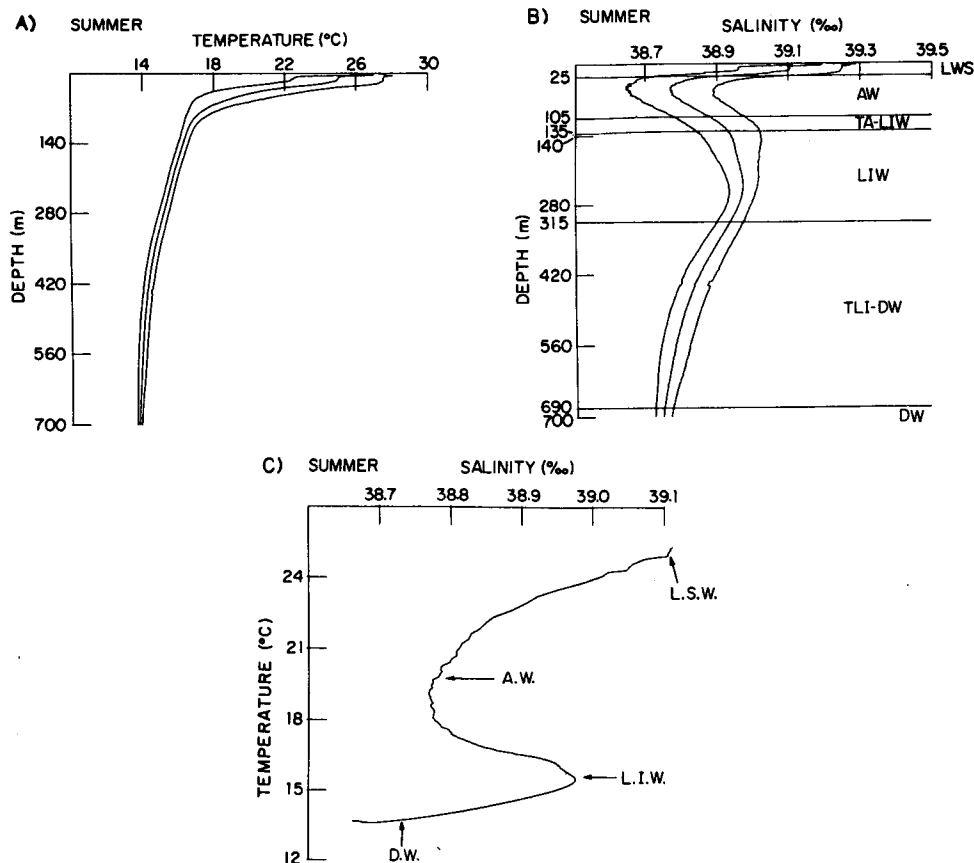
FIG. 9. As in Fig. 7 but for summer cruises average.

the clarity of the figures, the profiles are depicted only down to this depth.

The lowest surface temperatures of the series, about 16°C, were encountered during MC22, which was carried out in March in the middle of the oceanic winter. During this month the temperature is almost uniform from the surface to 500 decibars. The salinity profile exhibits a barely discernable minimum in the surface layers, at least in two of the four winter average profiles. The signature of the AW occurs within one standard deviation of the mean profile. The maximum of the LIW is quite conspicuous in the salinity profile as well as on the T-S diagram. Moreover, it appears to produce a slight inflection in the Brunt–Väisälä frequency profile, which is otherwise almost a straight line.

During the following months, as the temperature of the upper layers increases, we can observe the formation of the LSW and the seasonal thermocline. The surface layer temperature reaches its peak (27.2 ± 0.6°C) in August (during MC 18), when we can observe a shallow mixed layer extending to about 20 decibars and a very steep thermocline.

The increased heat and evaporation produce LSW that reach their peak salinity (39.45‰) at the end of the summer, during MC24 of October 1983. In parallel,

the minima of the AW become more conspicuous. Eventually, during the later part of the year, the LSW cools down and the two upper layers mix until they form the single water mass present during the winter season. One should be aware, however, that some of the fluctuations in the strength and depth of the AW minima, e.g., the change from MC14 to MC24 to MC15 (in Fig. 12 from 38.65 to 38.85 to 38.75‰), are due to the variability of the mesoscale eddy field between these cruises (see sections 5 and 6). Thus, if one looks at sequential cruises the changes appear to be more regular. From MC14 to MC15, September to November 1980, for example, the salinity minimum increases from 38.65 to 38.75‰; from MC18 to MC19, August to November 1981, the salinity minimum stays at the same level 38.75‰.

The entire process of surface water formation and mixing can be followed in the series of T-S diagrams and the Brunt–Väisälä frequency profiles in Fig. 12. As the LSW develops its identity and the density gradient between the LSW and AW increases, a shallow subsurface maximum develops in the Brunt–Väisälä frequency profile, indicating an increase in the stability of the two layers. This maxima reaches its peak (3.0 × 10⁻³ cps) in August and then diminishes toward the
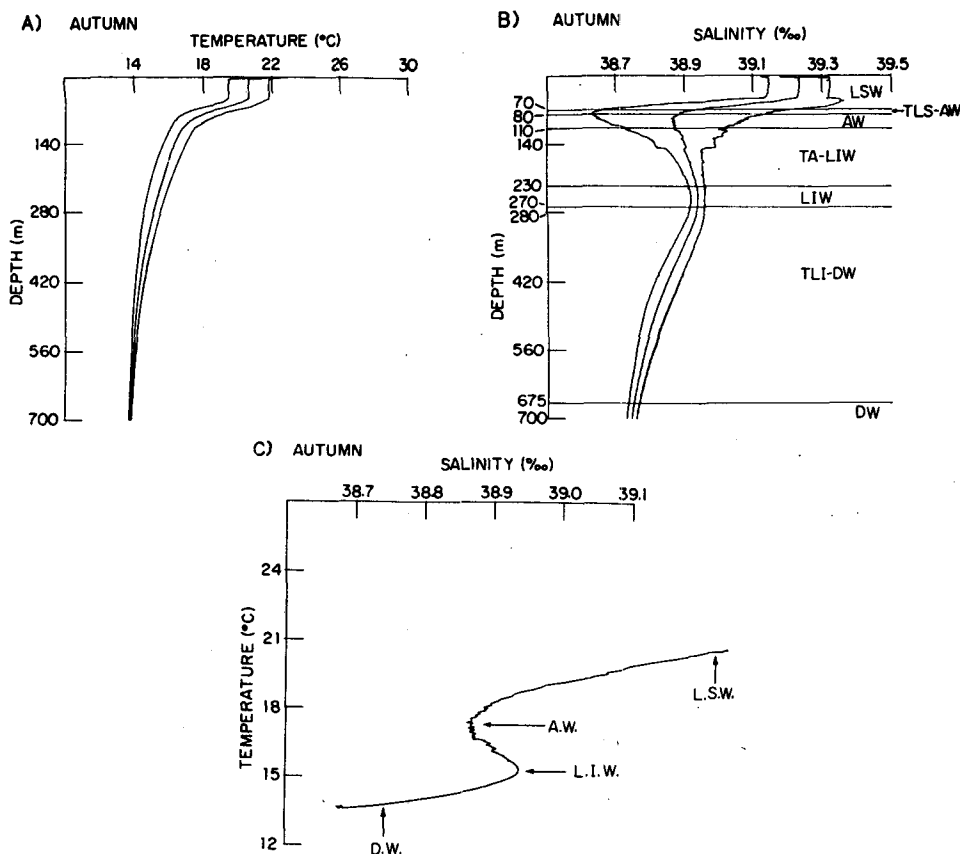
FIG. 10. As in Fig. 7 but for autumn cruises average.

winter, when it disappears and the profile becomes almost uniform from the surface to the bottom, e.g., cruise MC22 of March 1983. However, the other $N(z)$ winter profiles (MC11, MC25, MC16) show a discernable (but small in amplitude) thermocline maximum, between 200 and 300 m, which contributes to the $N(z)^2$ inflection shown in Fig. 6 at about the same depth.

Another conspicuous feature of the salinity profile as well as of the T-S diagram is the maximum related to the LIW. This feature is present throughout the year, changing very little in salinity and temperature from one month to another. MC20 presents the only anomalous salinity profile and T-S diagram. The salinity profile is almost uniform from the surface down to the LIW layer, and the T-S diagram is also indicative of the process of homogenization of the salinity properties. The temperature profile is not remarkably different from the others in the same period. As we will discuss later, between MC19 and MC20 a process of LIW formation has occurred, which has ventilated the salt properties of the layers of the upper main thermocline.

4. Dynamical and empirical modes

In this section we describe the vertical structure of the flow field via the study of the baroclinic dynamical

modes (DM) and empirical orthogonal functions (EOF). The DM are defined as the eigenfunctions, $\phi_n(z)$, of the vertical structure equation (Pedlosky 1979)

$$\left(\frac{f_0^2}{N^2(z)} \phi_{nz}\right)_z = -\lambda_n^2 \phi_n \tag{1}$$

with $\phi_{nz} = 0$ at $z = 0$, $z = 1600$ m, the latter corresponding to the average depth of the region. The subscript z indicates partial differentiation, f_0 is the value of the Coriolis parameter at the central latitude of the region (33.5°N), and $N^2(z)$ is the climatological Brunt–Väisälä frequency profile shown in Fig. 6. The eigenvalues of (1), denoted by λ_n^2 are the square of the inverse of the internal Rossby deformation radii, R_n. We solved (1) numerically using a shooting method with a vertical grid spacing of 8 meters.

The results are presented in Fig. 13 for the first three baroclinic DM; the Rossby radii of deformation are 12.4, 6.4 and 4 km. These small values of the internal Rossby radii are usually found between 50° and 60°N of latitude in both Atlantic and Pacific oceans (Emery et al. 1984). The first baroclinic DM has a zero crossing at 360 m and the second at 70 and 540 m. The shape of these baroclinic DM is similar to those of other regions (Smith et al. 1985; Pinardi and Robinson 1987;
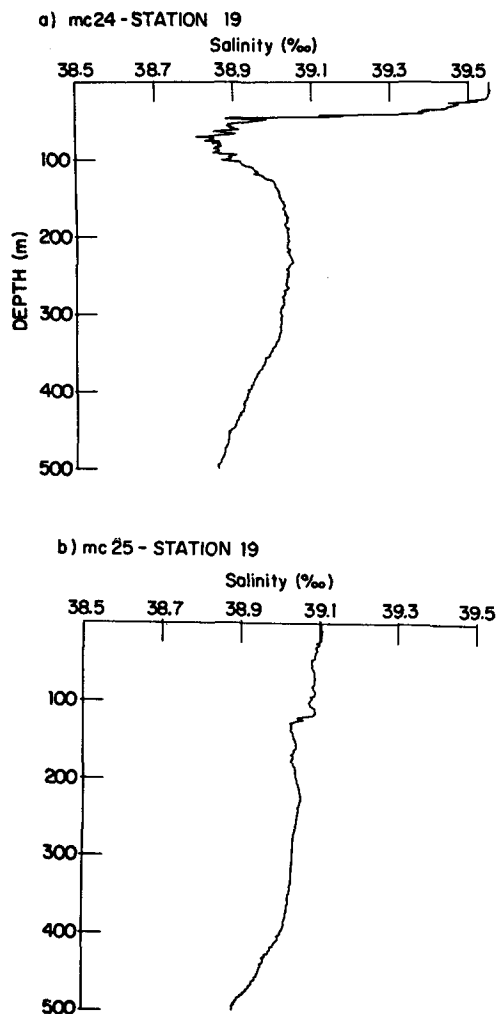
a) mc24 - STATION 19

b) mc 25 - STATION 19

FIG. 11. Salinity profile (a) for MC24 station 19 (summer) and (b) for MC15 (winter).

McWilliams et al. 1986); the first baroclinic DM is upper thermocline intensified, and the second has its maximum amplitude at the top of main thermocline (approximately 180 m). The zero crossings are quite shallow, corresponding to the relatively shallow thermocline structure of the region. The zero crossing of the first baroclinic DM approximately defines the bottom of the main thermocline (Fig. 6), which encompasses the LSW, AW and LIW layers. The second baroclinic DM has its maximum amplitude in the TA-LIW layer. Since such a layer is pervasive in the salinity structures previously discussed, we expect an enhanced role played by the second DM to explain the baroclinic variability of the mesoscale currents of this region (see section 5).

In order to use a high-resolution multilevel quasi-geostrophic model in the near future, we tried to solve the centered finite difference eigenvalue problem for (1) with the fewest vertical levels necessary to maintain

an accurate description of the λ^2 and ϕ_n as given by the highly resolved shooting problem. With eight levels located at 30, 80, 120, 160, 230, 330, 490 and 1100 m, the eigenvalues are calculated to be 12.7, 6.6 and 4.1 km for the first, second and third baroclinic DM, respectively. Moreover, the vertical shape of the first two vertical modes is well reproduced with respect to the highly resolved shooting problem. Thus, we consider eight levels sufficient to describe the major features of the average stratification of the region, and these are used to describe the flow field throughout the paper.

The EOF are a set of orthonormal functions in the interval between the surface and the average bottom of the region. It can be shown via the calculus of variations (Kutzbach 1967) that the EOF representation is optimum, in the sense that maximum variance may be accounted for by choosing in order the eigenvectors associated with the largest eigenvalues of the appropriate covariance or correlation matrix (Lorenz 1956). Here we calculated the EOF of the geostrophic pressure field in two different ways: the first uses pressure deviations from the horizontal average (EOF), as has been widely done in oceanography (De Mey and Robinson 1987; Smith et al. 1985); the second uses pressure deviations normalized by the standard deviations (NEOF) and has been used more commonly in meteorology (Lau 1981).

We start from the geopotential anomaly defined by

$$\Delta D = -\int_{P_{ref}}^{P} \frac{1}{\rho(x, y, S, T, P')} - \frac{1}{\rho(35, 0, P')} \, dP',$$

where P_{ref} is the pressure reference depth chosen to be 700 m; ρ is the density profile at each x, y station and P is the pressure corresponding to each of the eight levels described above. The reference level at 700 m was chosen because it is the deepest level for which there are 25 to 30 stations for each cruise (see Table 1); hereafter we exclude MC11 because it has too few stations. It is also the top of the DW layer, in which it is reasonable to expect the baroclinic currents to go to zero. We transform the geopotential anomaly in geostrophic streamfunction, ψ, by using the relationship $\psi = \Delta D/f_0$, dimensionally. This geostrophic streamfunction contains only the baroclinic part of the flow field and is then defined up to the unknown barotropic part of the total current field. We nondimensionalize the streamfunction field by the factor $U_0 L_0$, where U_0 is the typical velocity scale equal to 1 cm s^{-1} and L_0 is the horizontal scale length chosen to be 15 km or approximately the first internal Rossby deformation radius. Furthermore, we define the streamfunction deviations at each level $l = 1, \cdots, 8$ as $\psi_l(x, y, t) = \psi_l(x, y, t) - \{\psi_l(t)\}$, where $\{\psi_l(t)\} = N^{-1} \sum_l^N \psi_l(x_i, y_i, t)$ and N is the number of stations in each single cruise or in the total dataset. To calculate the EOF we consider only the stations at which we have at least eight levels of data: N varies between 18 and 25 for each cruise and is about 360 for the whole dataset.
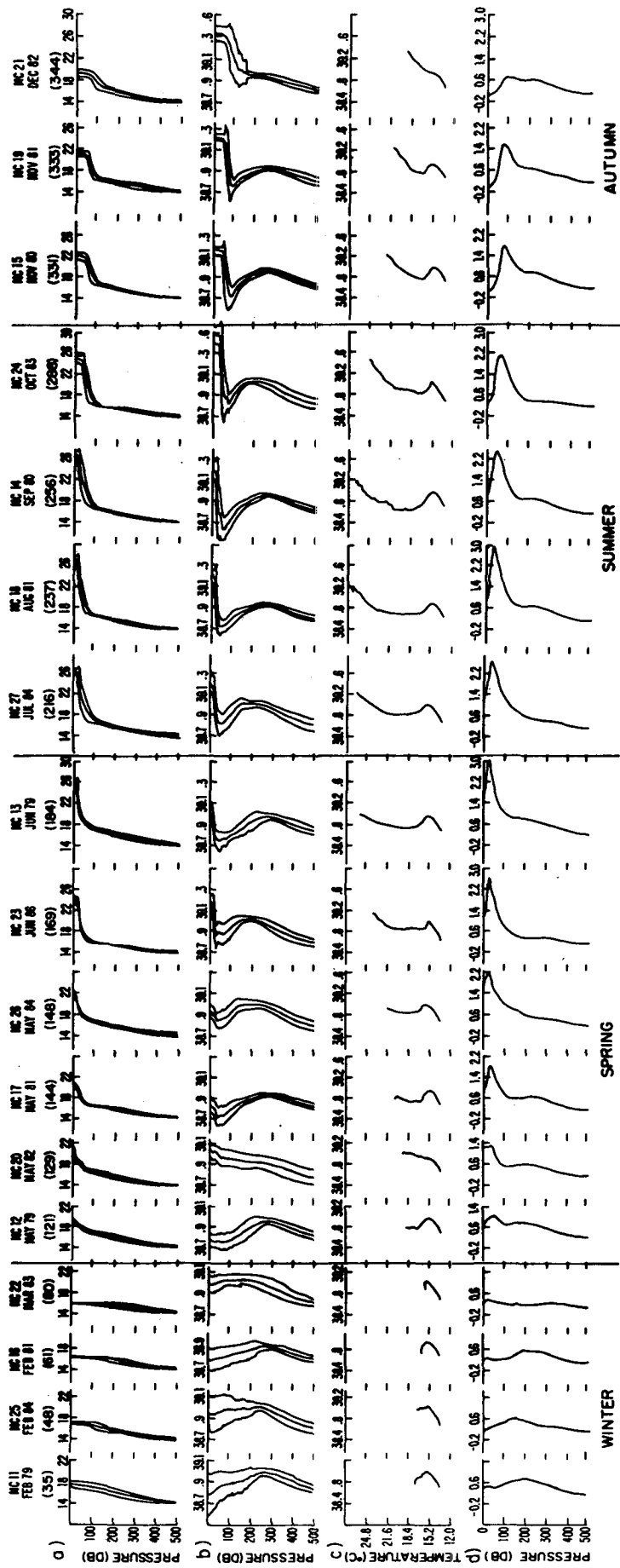
FIG. 12. Temperature (a) and salinity (b) profiles, T–S diagram (c) and N(z) (d) profiles for each cruise. Units are °C for T, ‰ for S, and cycles per second for N(z). The parenthetical numbers (top) indicate the day in the year taken to be the central day of each cruise duration.
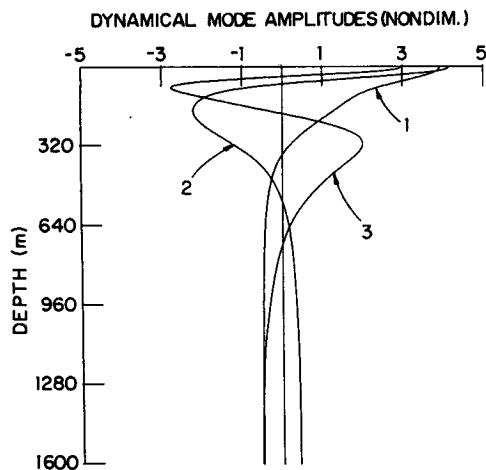
DYNAMICAL MODE AMPLITUDES (NONDIM.)

FIG. 13. Dynamical mode amplitudes for the first (1), second (2) and third (3) eigenvectors of Eq. (1).

The first EOF method considers the covariance matrix

$$C_{IJ} = \frac{\{\psi_I \psi_J\}}{N} \qquad (2)$$

with $I, J = 1, \cdots, 8$ levels. The eigenvectors of this matrix are the EOF decomposition of the vertical shear of the flow field; they take into account both the correlation and the different variance at the selected levels.

If we normalize the N measurements by their standard deviation at each level, we obtain instead of (2) a correlation matrix.

$$C_{IJ} = \frac{\{\psi_I \psi_J\}}{N\sqrt{\{\psi_I^2\}\{\psi_J^2\}}} . \qquad (3)$$

We call NEOF the eigenvectors of (3). The use of normalized variables ensures that each level is of equal importance in determining the form of the representation. This weighting procedure (normalization) prevents the first eigenvectors from being dominated by the levels with largest variance.

In Fig. 14 the EOF of each single cruise horizontally averaged vertical profile is presented as a function of depth. Figures 14a, b show the first and second EOF. The first EOF has a surface and middle thermocline intensified signature. The second EOF profiles are TA-LIW/LIW intensified and sometimes also bottom intensified. Using the total number of stations in the dataset we calculated the climatological EOF shown in Figs. 14c, d. These profiles are centered around a mean value of the single cruise EOF. In Table 3 the percentage of variance accounted for by the first and second EOF at each level is listed. Down to 160 m (level 4) the first EOF accounts for more than 90% of the variance with the exception of four cruises (MC14, MC15, MC24, MC25) where the contribution of the second EOF starts to be as high as 15%–50%. At the LIW levels (5–6) the second EOF accounts for more than 25% in the same

four cruises and about 10%–20% for the rest. Below the thermocline (levels 7–8) the first and second EOF share about the same contribution in variance; moreover the total variance accounted by the sum of the two EOFs can be as low as 5%–50%. In conclusion, at the lower levels the second and higher EOF modes become as important as the first EOF mode in describing the variance of the profiles. This is due to the large difference between the variance at the upper and lower thermocline levels, so that the covariance matrix is dominated in the first eigenvectors by the upper thermocline levels. With this representation, any extrapolation of the near surface information down to 1100 m using only the first and second EOF is subject to large errors.

In Fig. 15 we show the climatological and cruise by cruise NEOF. The shape of these eigenfunctions is very different from the EOF of Fig. 14 since this time, all the levels are weighted equally. The first NEOF shows that variability is highly correlated between the AW and the TLI-DW layers (80–490 m) and anticorrelated with the DW layer (1100 m). The second NEOF is more variable between cruises than the EOF and is generally lower-thermocline intensified. The variances accounted for by these NEOF are shown in Table 4. The first EOF accounts for more than 90% in all the cases down to 330 m, and the second becomes comparable to the first NEOF at 1100 m. Even at 490 m (level 7) the second NEOF accounts, at maximum, for about 10% and only for three cruises (MC12, MC14, MC25). The sum of the first and second NEOF accounts for more than 90% of the variability at all levels. The first climatological NEOF (Fig. 15c) accounts for more than 90% down to 330 m and only 60%–80% deeper; in this representation the sum of the two climatological NEOFs accounts for about 84% of the variability at 1100 m.

In summary, the EOF analysis shows that the baroclinic flow is upper-thermocline intensified and that the baroclinic shear is contained in the first 330 m of the water column. The second EOF shows a TA-LIW intensified signature. In the LIW layer the variance accounted for by this EOF can be as high as 20%–50%. The sum of these EOF cannot account for the variance at 1100 m for the reasons explained before. The NEOF are shown to be a complementary view of the vertical variability of the eddy field: the combination of the first and second NEOF can explain over 95% of the variance at all the levels.

In conclusion, we have calculated the percentage of EOF energy contained in each DM. We can do this because the EOF are an orthogonal and complete set of eigenfunctions over which we can expand any other vertical shape. In this case we expand the DM of our system. The first baroclinic DM contains 82% of the energy of the first EOF while all the others account equally for the rest. The second baroclinic DM contains 92% of the energy of the second EOF.

a) FIRST EOF

b) SECOND EOF

c) FIRST CLIMATOLOGICAL EOF
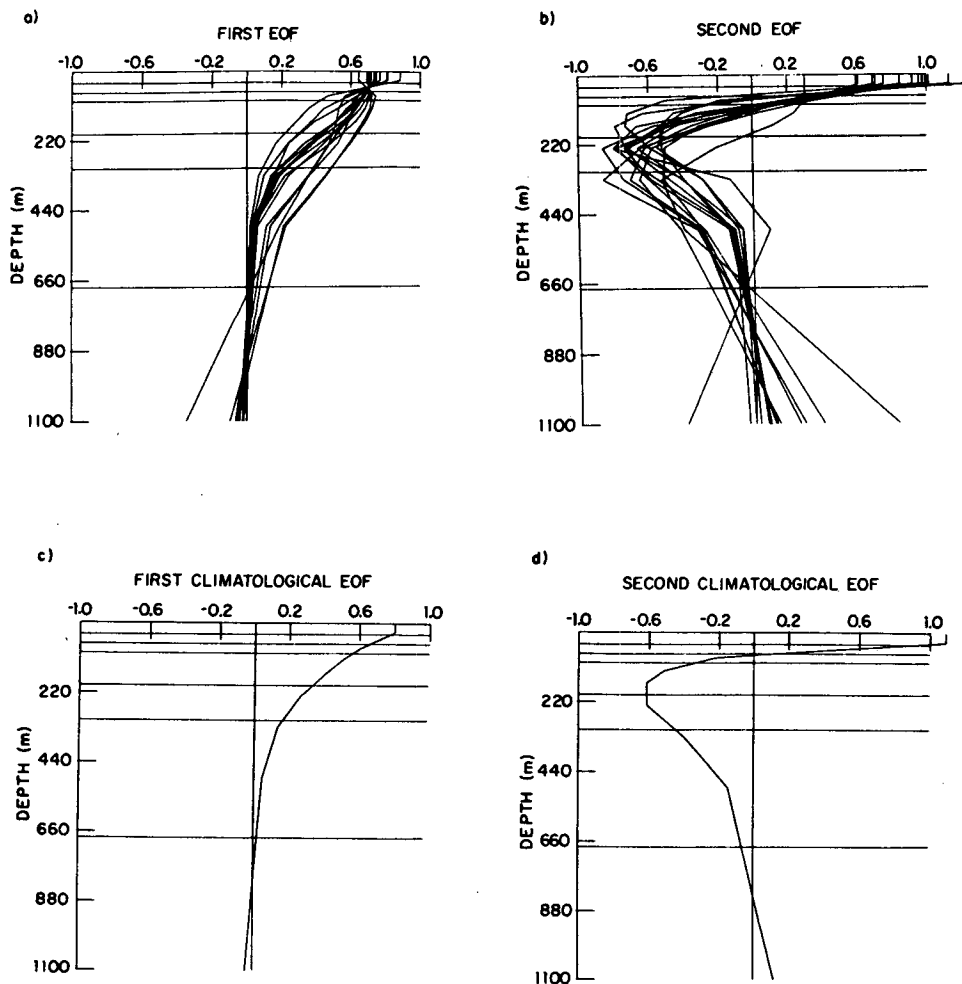
d) SECOND CLIMATOLOGICAL EOF

FIG. 14. First (a) and second (b) EOF for each cruise (MC12-MC27). Climatological (c) first and (d) second EOF. The horizontal lines indicate the layer depths as computed in Fig. 4c, d.

5. Space and time scales of the geostrophic flow field

In this section present the objective mapping of the streamfunction ψ at the eight levels described in section 4. For each cruise the stations used (see Table 1) are at least 700 m deep, but not all of them reach 1100 m. Thus, we extrapolated the streamfunction into the deepest level using a least squares projection method on the NEOF amplitudes. We use the individual cruise NEOF and not the climatology NEOF since the second one varies appreciably, both in amplitude and in variance, from one realization to the next. The result is that we can form eight levels of baroclinic streamfunction for each cruise at all the stations for which we have information down to 700 m. This dataset is used in the present paper for the kinematic description of the flow field and will be used in the future for model initialization and dynamical studies. In the Appendix the procedure of extrapolation is explained in detail.

The $\psi(x, y, z, t)$ data are objectively analyzed using an isotropic, homogeneous and steady correlation function of the form (Carter and Robinson 1987)

$$C(r) = \left(1 - \frac{r^2}{a^2}\right) \exp\left(-\frac{1}{2}\frac{r^2}{b^2}\right)$$

with $r^2 = x^2 + y^2$.

The domain size is 220×270 km^2 in the longitudinal and latitudinal directions (see Fig. 1b) and the interpolation grid size is 5 km. The parameters a and b are chosen to be 60 and 40 km, since previous studies of this region (e.g., Robinson et al. 1987) have shown that these values give an accurate description of the mesoscale eddy field as revealed by a fine resolution mesoscale survey and suggest that even with this coarse resolution sampling, these correlation values produce the correct space scales of the mesoscale features. We calculate the streamfunction deviations $\psi^* = \psi - \langle\bar{\psi}\rangle$ from the global time and space average of the streamfunction field at each level, denoted by $\langle\bar{\psi}\rangle$. In

TABLE 3. Variance accounted by the first (1) and second (2) empirical orthogonal functions (EOF) at each level and for each cruise. "Climatic" means that all the stations are considered (~360).

Cruise	EOF	Level							
		1	2	3	4	5	6	7	8
MC12	1	98.8	99.7	99.9	98.4	92.3	78.3	43.3	9.1
	2	1.0	0.3	—	1.2	7.5	19.4	32.6	31.5
MC13	1	99.1	99.9	1.0	99.4	96.4	91.9	94.7	86.5
	2	0.9	0.1	—	0.6	3.6	7.6	3.8	0.6
MC14	1	84.5	83.2	58.6	47.4	32.0	22.3	16.3	0.1
	2	15.5	15.9	41.3	52.4	66.9	73.0	67.0	32.1
MC15	1	94.1	99.9	92.1	84.5	71.9	57.9	50.3	41.2
	2	5.9	—	7.7	15.4	27.7	39.3	43.6	38.1
MC16	1	97.0	99.8	99.5	96.2	87.6	94.8	79.7	25.9
	2	2.9	0.2	0.5	3.7	11.9	2.1	9.4	52.0
MC17	1	94.7	99.7	99.6	97.9	91.5	77.9	68.2	24.4
	2	5.3	0.2	0.3	2.0	8.3	21.0	21.7	17.0
MC18	1	84.3	99.1	96.0	92.5	82.9	72.9	63.0	26.2
	2	15.7	0.7	4.0	7.5	16.6	25.6	26.5	5.4
MC19	1	93.9	99.6	99.5	98.4	94.2	88.6	88.1	5.8
	2	6.0	0.3	0.4	1.5	5.6	9.8	9.1	—
MC20	1	98.9	99.2	99.3	99.3	96.0	72.0	49.7	41.1
	2	0.5	0.7	0.6	0.1	2.4	26.9	49.9	57.0
MC21	1	96.8	99.6	99.2	98.1	93.3	83.0	80.5	50.7
	2	3.1	0.2	0.6	1.9	6.4	14.4	13.6	9.7
MC22	1	97.6	99.6	99.9	99.3	94.7	74.9	56.0	11.0
	2	2.3	0.3	—	0.6	5.2	24.3	40.8	69.0
MC23	1	88.2	98.6	99.6	97.3	90.4	77.0	64.1	38.3
	2	11.8	1.4	0.3	2.6	9.6	22.6	34.4	44.8
MC24	1	60.4	97.8	82.4	77.2	74.2	72.0	71.6	44.7
	2	39.6	1.6	17.3	22.7	25.6	25.8	22.4	37.1
MC25	1	90.8	98.8	98.2	78.9	38.9	26.6	19.2	14.1
	2	9.1	1.1	1.3	20.7	60.8	72.6	77.5	82.2
MC26	1	90.7	98.5	99.8	99.1	94.8	89.4	81.8	68.9
	2	9.0	1.4	—	0.8	5.2	10.2	16.2	8.1
MC27	1	74.4	98.0	99.4	97.0	91.0	83.7	73.2	63.6
	2	25.0	1.8	—	2.6	8.8	14.5	19.3	30.3
Climatic	1	84.8	97.4	90.2	82.0	64.2	46.4	33.8	22.6
	2	15.0	1.2	9.2	17.7	32.3	39.6	33.9	15.8

Fig. 16 the ψ^* field is presented for level 5. We show this level (230 m) because it is well within the main thermocline region (Fig. 6) and shows no qualitative differences with the 160 m level, which is in the seasonal–main thermocline transition region.

The flow field immediately reveals the presence of strong mesoscale eddies embedded in a broader scale flow field (see MC12, MC13, MC15, MC17 and MC18), which filaments and meanders around them. The domain contains two to three eddies with a wide variety of space scales from a diameter of ~100 km or greater to smaller scales of the order of 60–70 km.

Moreover, we find periods in which the flow is populated by a single eddy center (MC19 and MC24–MC27). We divide the 16 cruises into three periods: the first from MC12 to MC21, in which the flow field shows several eddy centers and sometimes a discernible northeastward general circulation flow coming either from the western or southern side of the domain; the second from MC22 to MC23, which shows a much more quiescent flow field and smaller spatial scale variability (~60–70 km in diameter); and the third from MC23 to MC27, which is dominated by a single eddy center and a very weak cyclonic general circula-

a)

FIRST NORMALIZED EOF

b)

SECOND NORMALIZED EOF

c)

FIRST CLIMATOLOGICAL NORM. EOF

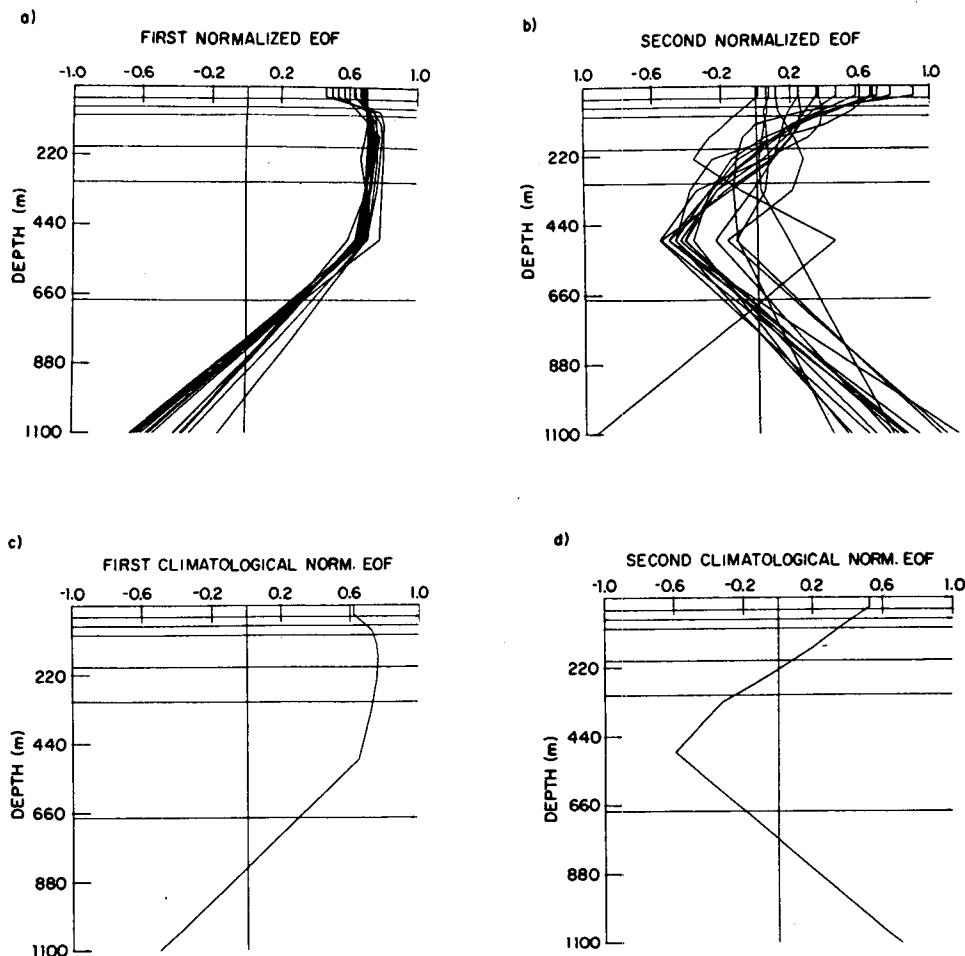d)

SECOND CLIMATOLOGICAL NORM. EOF

FIG. 15. As in Fig. 14 but for NEOF.

tion transport throughout the region. We now proceed to describe the variability in the three periods.

The first period shows the largest pressure perturbations (MC12, MC13, MC16, MC19, MC20); between the surface and 230 m, the vertical shear can be as high as in the case of MC13 (Fig. 17a) or weaker as for MC19 (Fig. 17b). In this period there is always visual coherence between the flow at 80 and 490 m, and the flow at 230 m except for MC12, MC14 and MC20 as shown in Fig. 18 (compare Fig. 16 with Fig. 18a). MC14 shows a qualitatively different picture at the surface than at depth, and MC20 shows almost no signature of the anticyclonic eddy at 490 m (Fig. 18b), while a dipolar structure (a high/low eddy pair) is evident at 230 m. During this period, the anticyclonic eddy in the northwestern side of the domain persists for over a season near the seamount of Fig. 1b. The velocity field for MC13 is shown in Fig. 19. This period shows the strongest upper thermocline currents in the jets at the border of the eddies: 30–40 cm s^{-1} at 80 m, 20 cm s^{-1} at 230 m, and 2.5 cm s^{-1} at 490 m.

MC19 and MC20 show some of the most interesting

and singular eddy fields in the first period. In Fig. 16, MC18 shows an anticyclone located near the center of the domain and one similar to the anticyclonic eddy present from MC12 in the northwestern corner of the domain. From MC18 (August 1981) to MC19 (Nov-Dec 1981) the flow changes qualitatively: the northwestern eddy weakens, and at the center of the domain only an isolated round eddy is left with an almost quiescent ocean surrounding it. We note that the circular shape of this eddy is well resolved by the data, since a few more stations were carried out between station 21, 26 and 22 of Fig. 1b to define the extent of the eddying motion. On the southern edge of this feature only a weak low pressure center is present. Five months later (MC20), the high pressure center has weakened (by a factor of ∼2), and it has paired with a cyclonic eddy at its southeastern border. The cyclonic eddy is small in diameter, and its vertical extension and strength is shown in Fig. 18b. The jets between and around the two eddies are of the order of 30 cm s^{-1} at 80 m and 5 cm s^{-1} or more at 490 m (Fig. 19).

The second period is remarkably different from both

TABLE 4. Variance accounted by the first (1) and the second (2) normalized empirical orthogonal functions (NEOF) at each level and for each cruise. "Climatic" means that all the stations are considered (~360).

Cruise	NEOF	Level							
		1	2	3	4	5	6	7	8
MC12	1	96.3	96.7	97.6	98.2	98.8	97.9	84.6	47.3
	2	2.5	2.8	2.3	1.6	0.4	0.9	14.9	50.9
MC13	1	98.7	99.3	99.5	99.6	99.1	98.2	98.9	89.1
	2	0.1	0.1	0.2	0.4	0.6	0.3	0.2	10.8
MC14	1	61.1	92.4	98.1	99.0	98.6	96.1	87.8	30.4
	2	30.2	7.2	1.7	0.5	0.1	2.9	11.6	61.7
MC15	1	90.2	96.0	98.9	99.4	99.3	97.8	95.5	82.7
	2	8.7	3.7	0.9	0.3	—	1.3	4.0	14.0
MC16	1	98.6	99.1	98.8	97.7	95.0	98.5	92.9	56.1
	2	0.0	0.2	1.0	2.2	4.1	0.3	6.5	43.7
MC17	1	91.7	96.6	98.1	98.9	99.2	97.3	91.0	46.3
	2	6.3	2.9	1.8	1.0	0.2	0.9	7.7	51.3
MC18	1	84.9	98.5	99.5	99.7	98.9	97.0	89.6	64.4
	2	—	—	—	—	—	—	0.9	35.1
MC19	1	94.1	98.6	99.6	99.7	99.1	97.4	97.3	13.4
	2	0.2	—	—	—	0.1	—	0.4	86.4
MC20	1	96.6	96.7	96.8	97.3	98.8	96.5	89.4	84.1
	2	2.6	3.1	3.2	2.6	0.4	2.6	10.6	15.0
MC21	1	96.6	98.5	99.1	99.4	99.2	97.4	97.6	84.2
	2	1.0	0.6	0.4	0.3	0.1	—	1.0	14.3
MC22	1	94.5	96.8	98.0	98.9	99.7	96.8	90.4	47.6
	2	4.8	3.0	1.9	1.0	—	1.9	8.0	49.1
MC23	1	88.3	95.9	98.7	99.6	99.6	97.7	94.4	79.8
	2	10.7	3.9	1.2	0.3	—	1.4	4.9	17.0
MC24	1	65.5	97.9	99.5	99.5	99.4	99.0	98.0	89.1
	2	33.2	1.7	—	0.1	0.3	0.4	0.3	5.1
MC25	1	71.6	82.9	91.6	98.9	96.5	92.3	87.0	81.9
	2	27.9	17.0	8.3	0.8	3.1	7.4	11.9	16.4
MC26	1	91.0	97.0	98.8	99.6	99.4	98.2	95.4	81.8
	2	7.8	2.8	1.0	0.2	0.2	1.0	2.9	14.3
MC27	1	73.3	94.9	98.4	99.5	99.3	97.8	95.0	89.3
	2	25.3	5.1	1.3	—	0.6	2.0	4.1	8.8
Climatic	1	81.1	94.2	97.0	97.9	96.5	92.8	85.6	62.3
	2	10.5	4.9	2.7	1.2	—	3.3	13.0	22.3

period 1 and 3. Figure 18a and Fig. 16 show the vertical contrast of this flow field: the small eddies have a middle thermocline intensified signature, and no discernable northward general circulation transport is present. Moreover, the flow field evolves from MC22 to MC23 in a much more chaotic way and no clear connection can be made between the two different realizations, while before, for the same time lag (see MC12 and MC13), the flow was more temporally coherent. In section 6 we will see the anomalous water mass distribution of this mesoscale eddy field.

In the third period, an eddy center with a diameter somewhat larger than 100 km persists in the northeast corner for almost a year. Its vertical extension is remarkable, being a strong pressure anomaly down to 490 m (see Fig. 18b). In Fig. 19 the velocity field is shown for MC26. The swirl speed in the first 200 m is of the order of 10–20 cm s^{-1} and 5 cm s^{-1} at 490 m. It is the second highest velocity at this depth after MC20. The shape of this eddy changes between MC24–25 and MC26–27: it seems to oscillate between a slightly elliptical and circular shape, and a high pressure center is sometimes excited at its border during MC24 and MC27.
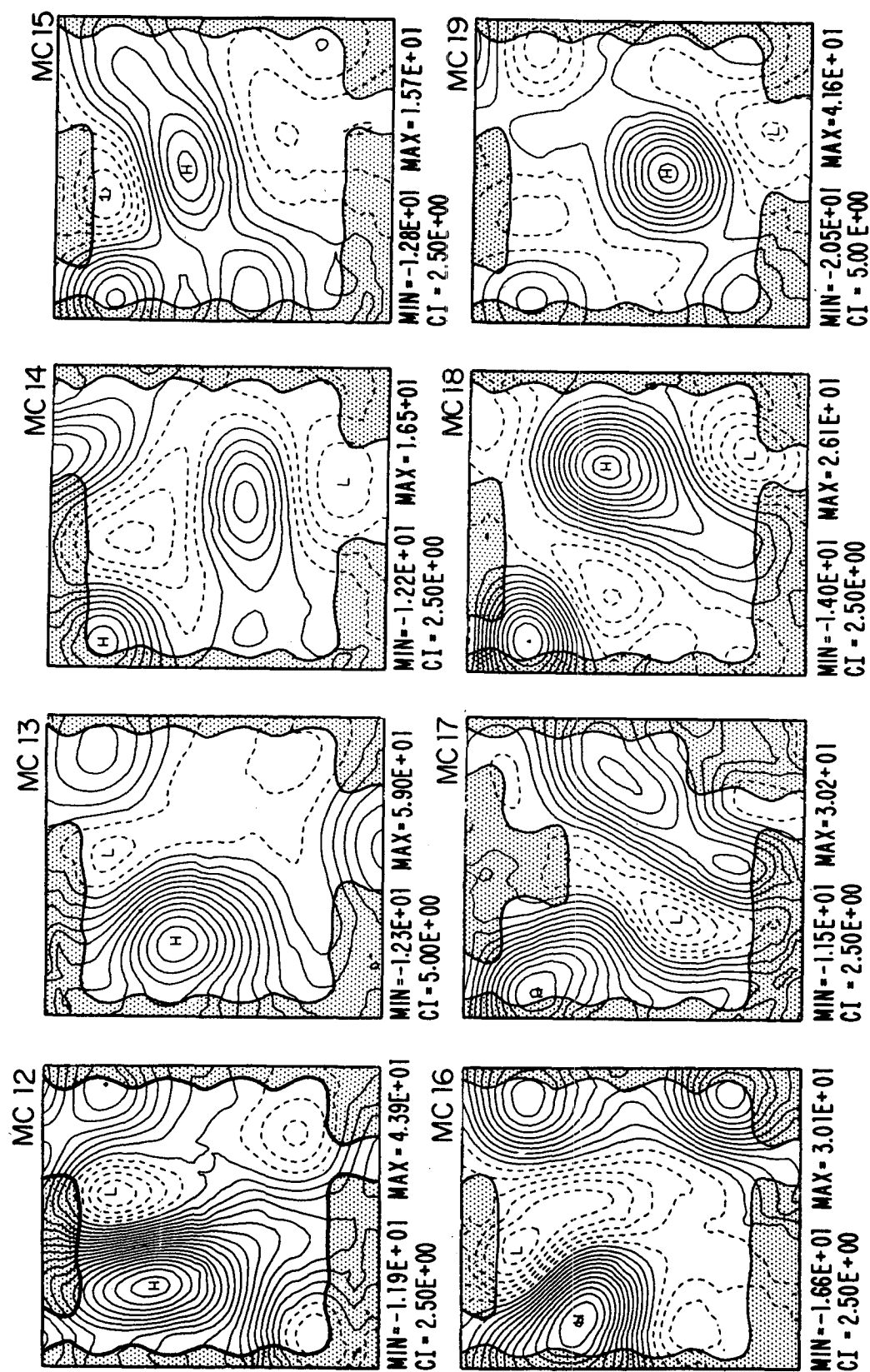
FIG. 16. The ψ^* field at level 5 (230 m) for each cruise: the cruise number is indicated above each map. The values are nondimensionalized by U_0L_0 (see text). The shaded areas indicate error variance greater than 40%. The min, max and CI below frames indicate the minimum, maximum and contour interval values.
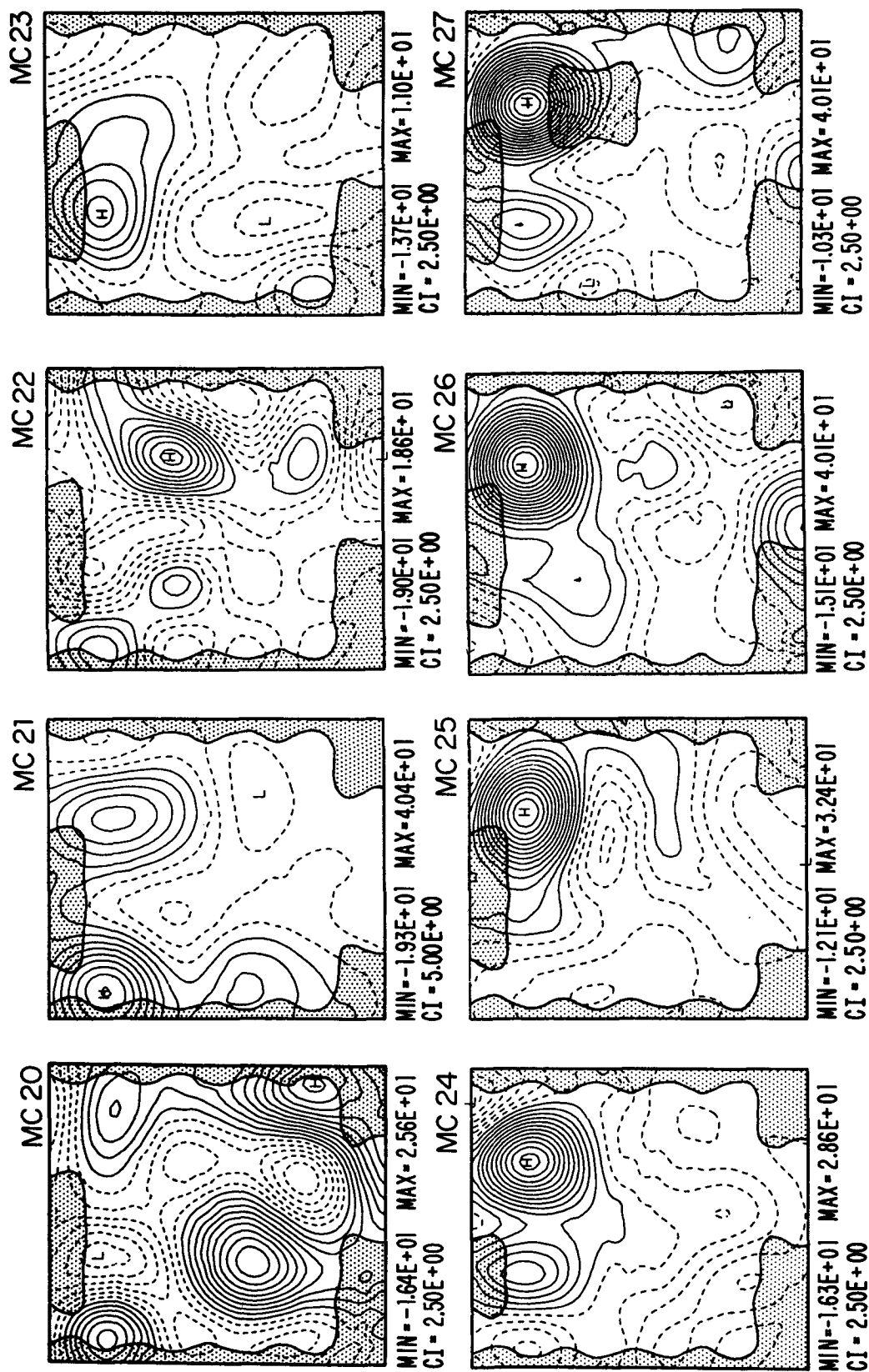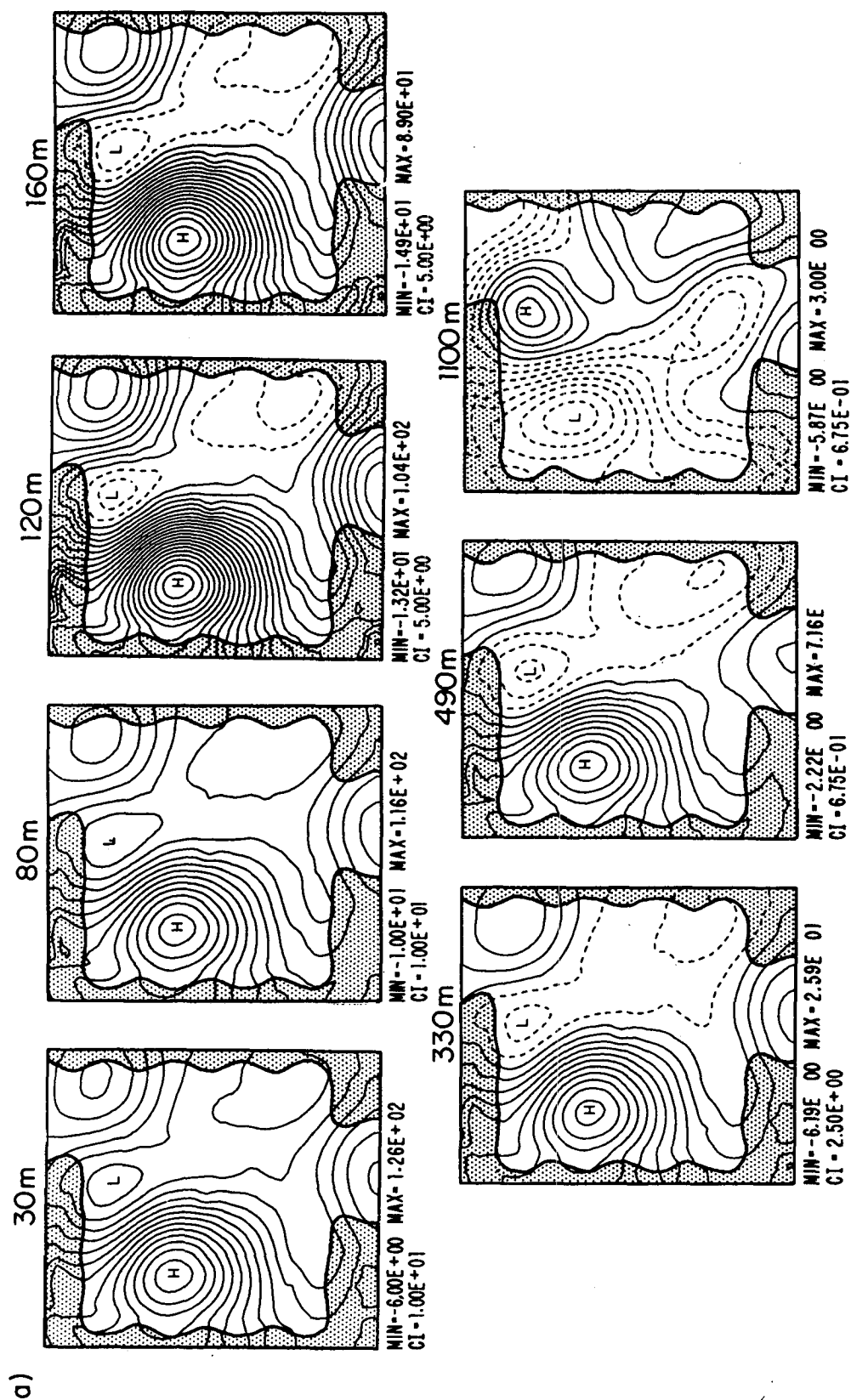
MC15 MIN=-1.28E+01 MAX=1.57E+01 CI = 2.50E+00

MC19 MIN=-2.05E+01 MAX=4.16E+01 CI = 5.00 E+00

MC14 MIN=-1.22E+01 MAX=1.65+01 CI = 2.50E+00

MC18 MIN=-1.40E+01 MAX=2.61E+01 CI = 2.50E+00

MC13 MIN=-1.23E+01 MAX=5.90E+01 CI = 5.00E+00

MC17 MIN=-1.15E+01 MAX=3.02+01 CI = 2.50E+00

MC12 MIN=-1.19E+01 MAX=4.39E+01 CI = 2.50E+00

MC16 MIN=-1.66E+01 MAX=3.01E+01 CI = 2.50E+00

MC 23

MC 22

MC 21

MC 20

MIN=-1.37E+01 MAX=1.10E+01
CI = 2.50E+00

MIN=-1.90E+01 MAX=1.86E+01
CI = 2.50E+00

MIN=-1.93E+01 MAX=4.04E+01
CI = 5.00E+00

MIN=-1.64E+01 MAX=2.56E+01
CI = 2.50E+00

MC 27

MC 26

MC 25

MC 24

MIN=-1.03E+01 MAX=4.01E+01
CI = 2.50+00

MIN=-1.51E+01 MAX=4.01E+01
CI = 2.50E+00

MIN=-1.21E+01 MAX=3.24E+01
CI = 2.50+00

MIN=-1.63E+01 MAX=2.86E+01
CI = 2.50E+00

FIG. 16. (Continued)

FIG. 17. (a) The ψ^* field for MC13 at depths indicated above the pictures. (b) As in (a) but for MC19.

FIG. 17. (*Continued*)

b)

a)

MC 14

MIN·-1.64E+01   MIN·4.27E+01
CI·5.00E+00

MC 22

MIN·-4.94E+01   MAX·1.24E+00
CI =5.00E+00

MC 23

MIN·-3.54E+01   MAX-7.21E+00
CI·5.00E+00

b)

MC 12

MIN·-2.53E+00   MAX·-6.58E+00
CI·6.75E-01

MC 20

MIN·-3.95E+00   MAX·1.28E+01
CI·1.35E+00

MC 25

MIN·-7.17E+00   MAX·1.71E+01
CI·1.35E+00
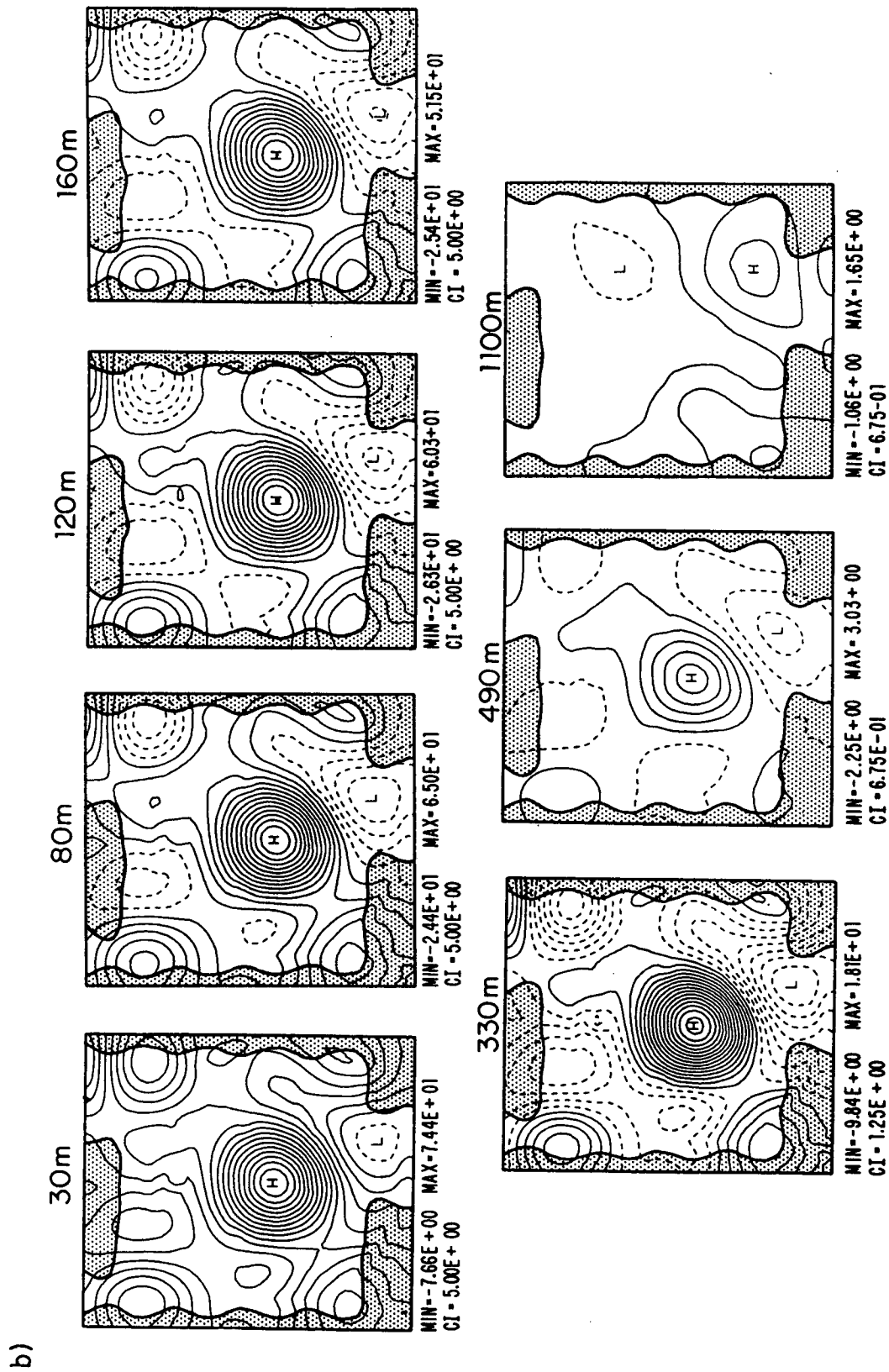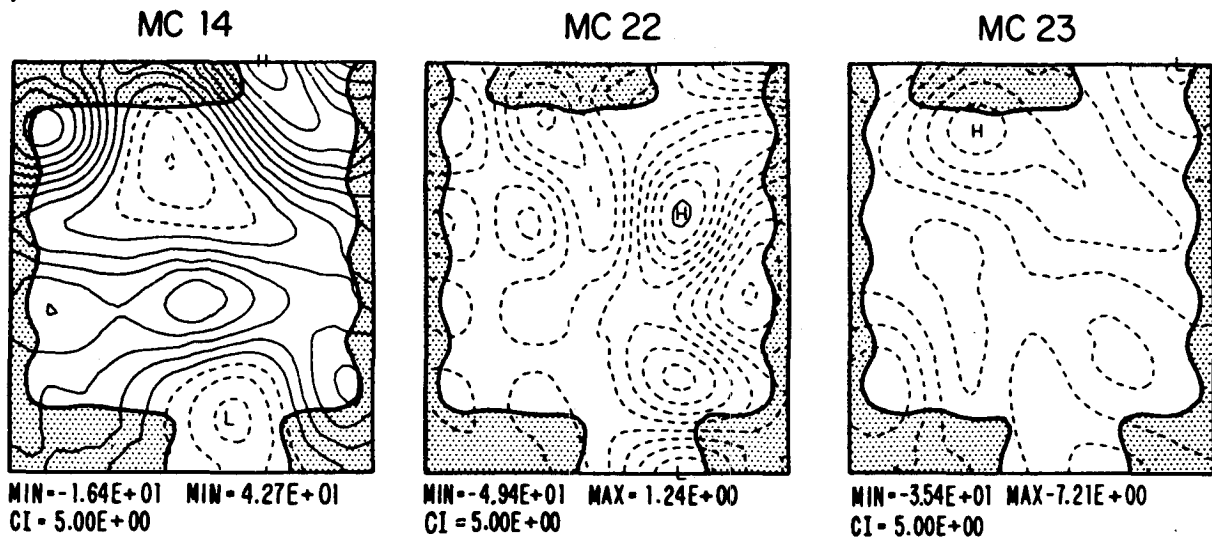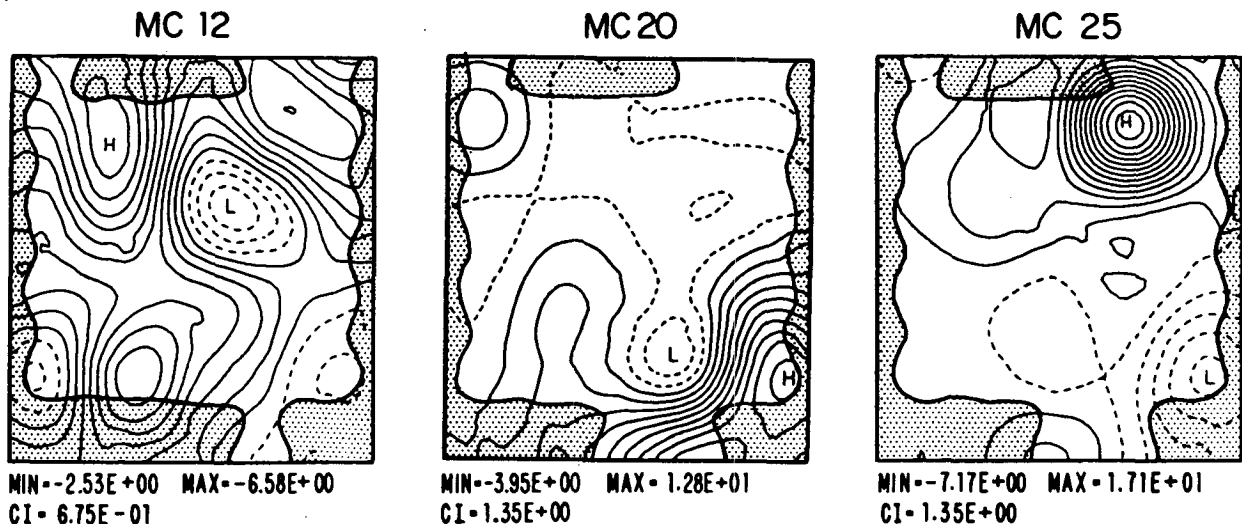
FIG. 18. (a) The ψ^* field for MC14, MC22, MC23 at 80 m. (b) ψ^* field for MC12, MC20, MC25 at 490 m. These fields should be compared with the maps of Fig. 16, showing the streamfunction at 230 m.

In conclusion, this flow field shows an energetic mesoscale variability never revealed before in this region. Furthermore, no clear seasonal variations in the strength of the flow field are recognizable, and the eddies persist in the region for more than a season. There are examples of isolated eddy centers with baroclinic velocities of the order of 20–30 cm s⁻¹ at 230 m. The horizontal structure of these isolated eddy centers is sometimes circular and extends throughout the main thermocline region.

Even though the dataset consists of almost five years of data, the persistence of this peculiar eddy field could
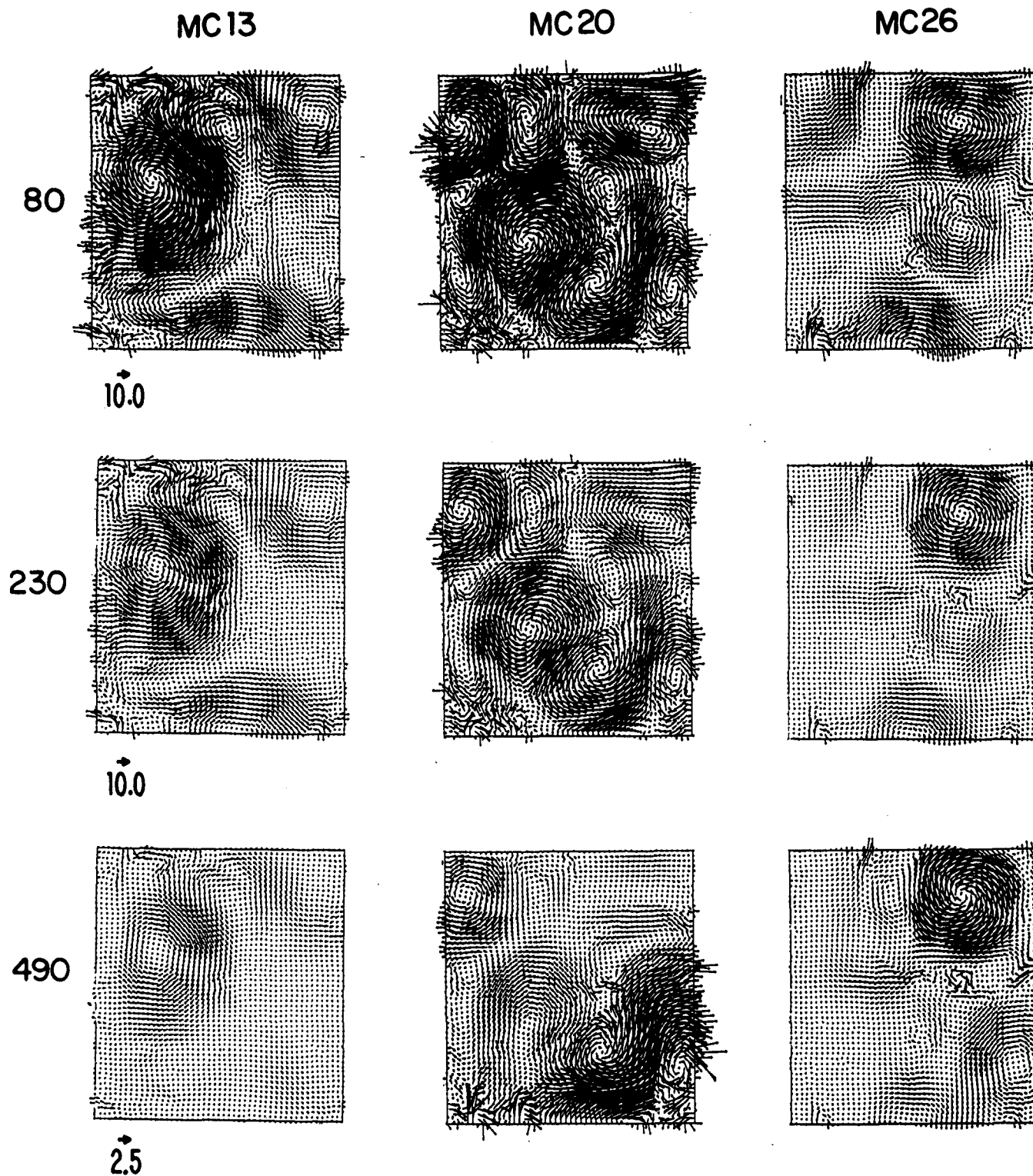
MC13   MC20   MC26

FIG. 19. Instantaneous velocity field for MC13, MC20, MC26 at 80, 230, 490 m. Arrows below pictures indicate velocity in cm s^{-1}.

highly bias the computation of an average velocity field. However we did calculate this average. Figure 20 shows the mean velocity structure as calculated by an arith- metic average of the velocities of all the realizations. The mean velocities range from approximately 10 cm s^{-1} at 80 m and 5 cm s^{-1} at 230 m down to 1 cm s^{-1}

$\vec{9.0}$ $\vec{5.0}$ $\vec{1.0}$
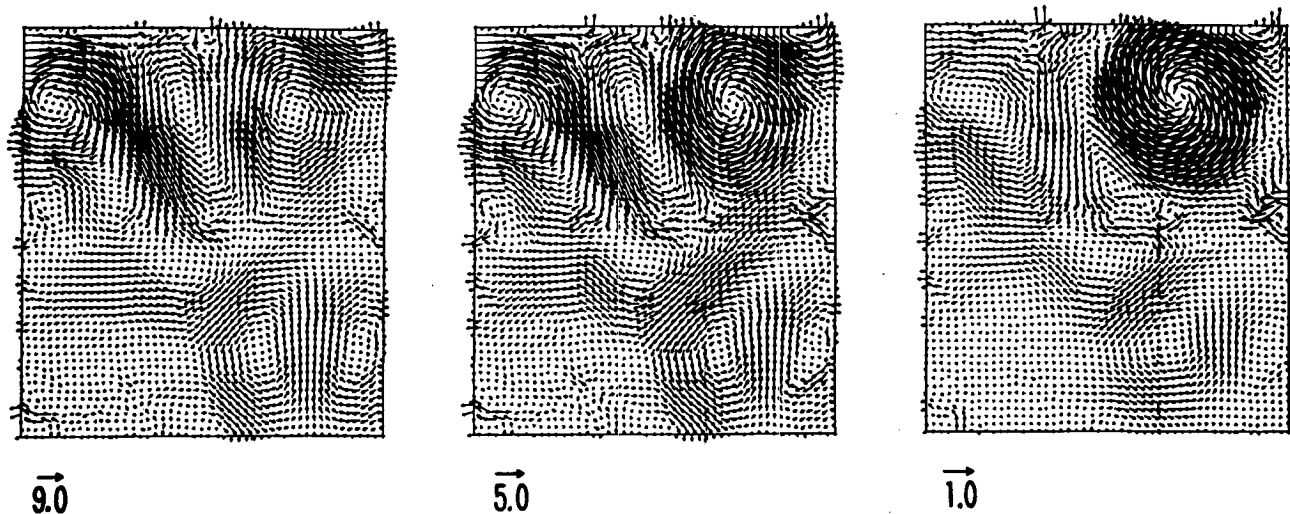
FIG. 20. Mean velocities at 80, 230, 490 m.

at 500 m. This picture shows that a possible surface-to-midthermocline northeastward transport is confined in the meandering jet located in the northern part of the domain. The deep flow (490 m) shows an eddylike structure due to the contributions of MC20 and the MC23–27 eddy fields. These mean flow features are not reconcilable with the general circulation flow direction indicated by Ovchinnikov (1966) (see Fig. 2). The persistence of this mesoscale eddy field makes it difficult to determine the background general circulation transport.

The emerging picture is that mesoscale variability dominates the instantaneous flow, deforming and sometimes masking the general circulation flow field we believe to be present in the filaments surrounding the eddies. The northeastward general circulation transport in Fig. 16 is perhaps present in the jet segments around the eddy borders. This variability is similar to other energetic mesoscale eddy fields present in the northwestern Atlantic (Hua et al. 1986; Pinardi and Robinson 1987) and in the California Current (Mooers and Robinson 1984; Robinson et al. 1986). This is the first time its presence has been acknowledged in this part of the World Ocean. Moreover, we further believe that this dataset shows a kind of mesoscale variability that is almost unknown and has never been captured in other open ocean regions. First, the eddies seem to have no significant westward propagation, appearing stationary in the time range of 2 to 3 months. Of course, we should expect slow Rossby wave phase speeds because of the small internal Rossby radius of deformation and the horizontal scales of the eddies (~100 km). If we calculate the first baroclinic Rossby wave period for a horizontal wavelength of 200 km, the result is ~900 days, i.e., more than twice the corresponding first Rossby radius of deformation wave period in the western North Atlantic. Topographic in-

teractions are expected to be important; the anticyclone in MC12 (Fig. 16) is located over the seamount of Fig. 1b, and this could explain its persistence in that part of the region. Second, some of the eddies show an extreme spatially coherent structure with very little ellipticity and a strong signature even below the main thermocline (490 m). Persistent monopole structures have been captured, lasting for over a season, in the same region.

6. Water mass structure of the eddy field

In this section we describe the distribution of the AW and LIW water masses within the eddy field described in the previous section. We identify the AW masses by salinity values less than 38.87‰ at 80 m and the LIW by salinity values greater than 38.94‰ at 230 m. We have chosen these two levels since in all seasons they are inside the layers that are characterized by these two water masses. Figure 21 presents maps of the salinity anomalies. We have chosen to show the maps for each season that present the two extreme distributions of water masses within the eddy field.

Figure 21a shows the winter conditions for MC22 and MC16. The AW is distributed around the high–low dipole of MC16 (see Fig. 16). We know therefore that AW is also present in the domain during winter. Due to its nonuniform horizontal distribution, it amounts to almost zero AW signal in the domain average profile of Fig. 12. In contrast, MC22 shows the total absence of AW at this level. Together with MC21, to be discussed later, it is the only example of such an anomalous high salinity field at 80 m. Moreover, this salinity anomaly structure shows a very smooth gradient that has no similarity with the small-scale geostrophic flow shown in Fig. 16 for the same cruise. At 230 m the LIW anomalies have a different structure

in the two cases: MC16 shows a tonguelike distribution of LIW around the border of the anticyclonic eddy in the northwestern side of the domain, while MC22 displays a small-scale pattern all above the limiting value of 38.94‰. Thus, the small-scale eddy structure of the geostrophic ψ field is due to the integrated contribution of the LIW intensified small-scale salinity eddies.

The spring conditions are shown for MC17, MC20 and MC23 in Fig. 21b. MC17 shows a large-scale salinity anomaly pattern of AW with small eddylike features embedded in it, similar to the case of MC16. MC20 presents a different picture with no AW in the domain and a positive salinity anomaly extremum located in the northeastern corner of the domain, where an anticyclonic eddy will appear distinctly during MC24 (see Fig. 16, MC24). The 230 m salinity field for MC20 shows very little LIW at this level, but an increase of salinity has occurred between 80 and 160 m, which has ventilated the salt properties of the upper layers of the thermocline in the position of the anticyclonic eddy (see Fig. 23). In contrast, MC17 shows weak anomalies of LIW distributed around the larger-scale eddy field. The other spring cruises (for example MC23) show patterns of salinity distribution with intermediate characteristics between these two extreme cases.

In Fig. 21c the summer conditions are shown for MC14 and MC27. MC14 shows a small-scale eddy field of AW that is unlike MC27, in which the AW is confined at the border of a large-scale positive salinity anomaly at 80 m. Thus, even in summer, the abundance of AW in the region is intrinsically coupled to the mesoscale eddy field. In this season, however, the tendency is generally that of MC14: AW anomalies embedded in a larger-scale eddy flow. At 230 m the LIW structure is either patchy (MC27) with strong salinity eddy anomalies or composed of weaker anomalies at the borders of the geostrophic flow field (MC14).

Autumn conditions are shown in Fig. 21d for MC21 and MC15. As usual these are two extreme conditions: MC21 shows no AW signal detectable above an anomaly value of 0.04‰ and MC15 shows a filamenting large-scale AW flow with small-scale positive and negative anomalies embedded in it (see also Fig. 16). Notice in MC21 the strong gradients of salinity along a jetlike feature meandering through the domain between higher and lower positive anomalies. The LIW consistently shows a more patchy pattern in strict spatial correlation with the ψ eddy field. MC21 contains the only few patches of high positive salinity anomalies, while MC15 has weaker LIW anomalies distributed around the eddy field of Fig. 16.

In summary, the abundance of AW in the domain is not directly connected to a particular season, and it is locally distributed in jets, filaments and patches. The LIW structures are always visually coherent with the streamfunction field variability, and the strongest anomalies are associated with the anticyclonic stream-

function centers. The process of AW intrusion into the domain can be followed in Fig. 21 by looking at the time sequence of MC21, MC23 and MC27 maps. MC21 (Fig. 21d) shows no AW present at 80 m. Six months later (spring), MC23 (Fig. 21b) shows small tonguelike negative salinity anomalies of AW entering from the southern part of the domain. A positive anomaly of salty water, a remnant of the northern side of the jet present in MC21, occupies the rest of the domain and will remain there for a year, as shown by MC27 (Fig. 21c). The positive anomaly in the northwestern corner corresponds to the anticyclonic pressure center present in the domain from MC24. The AW that has been intruding between MC21 and MC23 remains confined in the southern part of the domain without mixing or spreading with the northern high salinity core.

We now look at the vertical distribution of water masses within some of the eddy features shown in Fig. 16. Figure 22 shows a salinity and temperature cross section for MC12 across the anticyclone located in the northwestern side of the domain. The temperature cross section shows that the isotherms are depressed to at least 490 m, the depth at which we have a complete set of salinity and temperature measurements. Embedded in this temperature eddy field there is a core of LIW that extends ±50 m around 330 m, and jetlike low-salinity cores that cross the eddy at 80 m. The core of LIW is trapped within the eddy, which persists in the region for more than a season and is the deepest we could find in this dataset. Thus, the LIW trapped in this anticyclonic eddy is probably "old," or formed somewhere else and transported within the eddy into the domain. In Fig. 22 we have also displayed three salinity profiles at three stations centered across the eddy: the deep "core" of LIW is evident in each of them.

Figure 23a shows a cross section of MC19 anticyclone and Fig. 23b the corresponding maps for MC20. MC19 shows that, at the end of the summer, a high salinity core has formed at the surface levels. Weak (~38.94‰) salinity cores of LIW are evident in the position of the cyclonic circulation at depths of 160 and 330 m trapped inside the anticyclone. Furthermore, at about 80 m, centered in the anticyclonic eddy, there is a core of salinity minimum. Six months later (MC20, Fig. 23b) the picture has changed noticeably; in the position of the anticyclonic eddy the isohalines surface, and now the salinity is almost uniform from 80 to 160 m (it varies from 39.0‰ to 38.96‰). We think that this event is an example of an LIW "formation" process, which has "ventilated" the upper thermocline water masses in the position of the anticyclone. The salinity homogenization area is approximately 60 km in diameter, corresponding to the central core of the anticyclone. We observe that the salinity properties have been homogenized from the surface to ~200 m indicating mixing of the AW and LSW layers
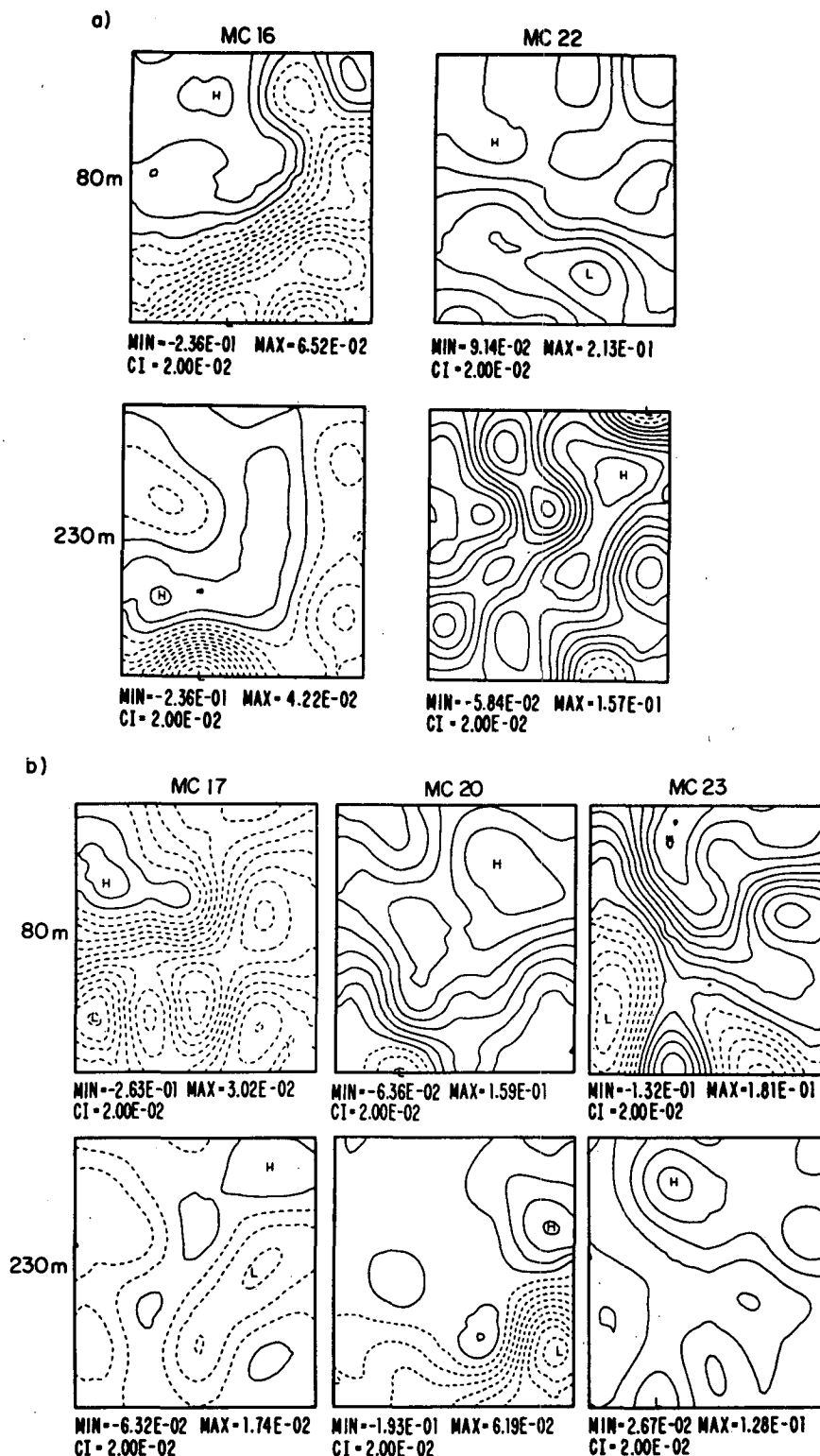
a)

MC 16

MC 22

80 m

MIN=-2.36E-01 MAX=6.52E-02
CI = 2.00E-02

MIN=9.14E-02 MAX=2.13E-01
CI =2.00E-02

230 m

MIN=-2.36E-01 MAX=4.22E-02
CI=2.00E-02

MIN=-5.84E-02 MAX=1.57E-01
CI=2.00E-02

b)

MC 17

MC 20

MC 23

80 m

MIN=-2.63E-01 MAX=3.02E-02
CI=2.00E-02

MIN=-6.36E-02 MAX=1.59E-01
CI=2.00E-02

MIN=-1.32E-01 MAX=1.81E-01
CI=2.00E-02

230 m

MIN=-6.32E-02 MAX=1.74E-02
CI=2.00E-02

MIN=-1.93E-01 MAX=6.19E-02
CI=2.00E-02

MIN=2.67E-02 MAX=1.28E-01
CI=2.00E-02

FIG. 21. Salinity anomaly distributions at two different levels, 80 and 230 m. The value subtracted is 38.87 at 80 m and 38.94 at 230 m. Positive (negative) anomalies indicate LIW (AW) at 230 (80) m, respectively. The min, max and CI below frames indicate the minimum, maximum and contour interval values. (a) Winter conditions for MC16 and MC22. (b) Spring conditions for MC17, MC20 and MC23.

c)

MC 14

MC 27

80m

MIN=-3.14E-01 MAX=-1.91E-03
CI=2.00E-02

MIN=-1.22E-01 MAX=2.18E-01
CI=2.00E-02

20m

MIN=-4.55E-02 MAX=4.20E-02
CI=2.00E-02

MIN=-7.87E-03 MAX=1.62E-01
CI=1.00E-02

d)

MC 21

MC 15

80m

MIN=-3.43E-02 MAX=5.11E-01
CI=4.00E-02

MIN=-3.43E-01 MAX=1.10E-01
CI=2.00E-02

230m

MIN=-3.20E-02 MAX=9.57E-02
CI=2.00E-02

MIN=-4.81E-02 MAX=3.10E-02
CI=2.00E-02
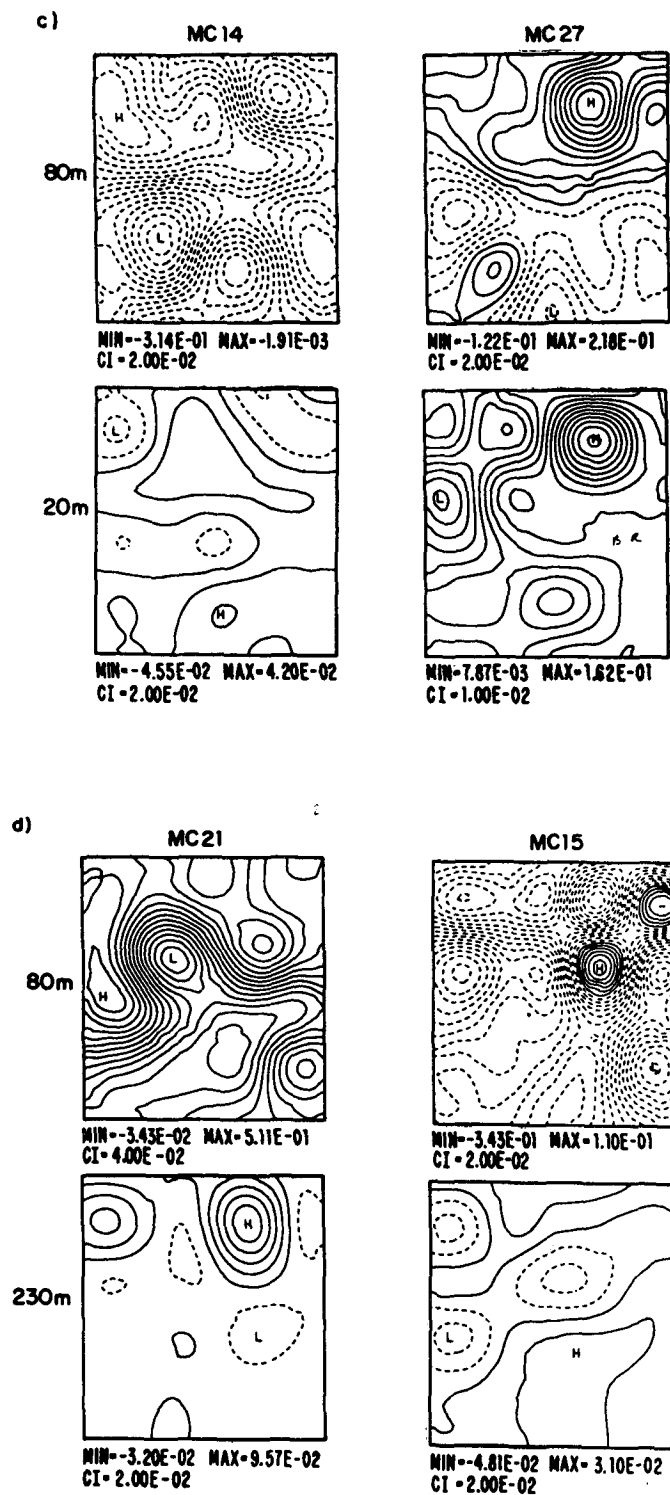
FIG. 21. (*Continued*) (c) Summer conditions for MC14 and MC27.
(d) Autumn conditions for MC21 and MC15.

present during MC19, which formed water with intermediate properties between the two (LIW). This unusual salinity distribution is also evident in the average

profile of Fig. 12. However, no strict conditions of vertical density homogeneity, are observed. Thus, either the density vertical mixing has occurred much earlier

STREAMFUNCTION MC 12

MIN=-1.19E+01　　MAX=4.39E+01
CI=2.50E+00

100km

MIN=1.41E+01　MAX=1.85E+01
CI=2.00E-01

TEMPERATURE (°C)

MIN=3.86E+01　MAX=3.90E+01
CI=2.00E-02

SALINITY(‰)

MC12 stations: 26 27 30
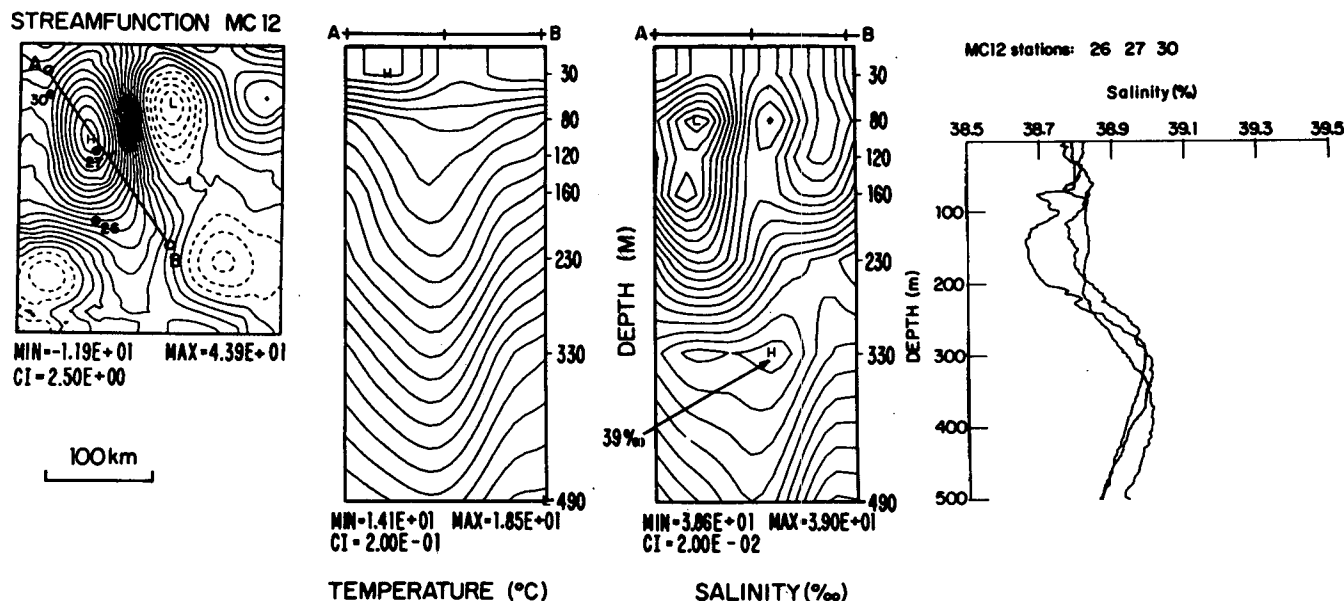
Salinity (‰)

FIG. 22. Cross section (A-B) of temperature and salinity for MC12. Left to right: streamfunction field at 230 m with the A-B cross section and stations 26, 27, 30 superimposed; isohalines as a function of depth along A-B; isotherms along A-B; salinity profiles at stations 26, 27, 30.

than at the time of MC20 or no convective overturning has occurred. In the first case, the typical "chimney" has not survived and stratification is quickly reformed inside the eddy. In the second case, the surface evaporation fluxes responsible for the increase in salinity of the LSW layer have not been enough to provoke the convective mixing, but other vertical diffusive instabilities could have homogenized the salinity properties, forming new LIW salty water.

Another example of LIW core trapped in the eddy field is given by the cross sections of Figs. 24a and 24b. The persistent anticyclonic eddy in the northeastern corner has a patch of LIW with salinity above 39.08 trapped around 160–230 m during the winter (MC25) and between 120–160 m during the summer (MC27). Since the depth of this LIW patch is closer to the surface than it was in the case of MC12 (Fig. 22), we think that this water could have been formed somewhere close to our domain shortly before this eddy entered the region of observation. In other words, this LIW has probably been formed more recently and has not yet sunk to greater depths as in MC12.

A series of T, S and σ_t profiles is shown in Fig. 25. The profiles were obtained at station 16, centered in the core of the anticyclonic eddy (see Fig. 1b), for MC24, MC25, MC26 and MC27. The temperature profile is almost homogeneous below 150 m, while above it we can see the seasonal changes induced by air–sea interaction processes. The salinity traces are also uniform, and large mixed layers are formed during the winter season down to 100 m. The σ_t profiles remain unchanged for almost a year below 150 m. Be-

tween 300 and 500 m, however, all the profiles show small changes in properties, a possible indication of mixing between the LIW and the TLI-DW layers. The waters of this eddy are more uniformly warm and salty than in any other eddy found in the region (compare with MC12, Fig. 22). This same eddy but for a different period is also described by Feliks and Itzikowitz (1987).

In conclusion, this analysis shows that the salinity field is dominated by eddylike structures. The more saline LIW is found to be generally trapped inside the anticyclones observed in the region. Furthermore, the vertical extent of the core of maximum salinity is of the order of 100 m, and it varies from eddy to eddy from a central depth of 330 up to 160 m. The smaller-scale eddies in the geostrophic streamfunction field (see, e.g., MC22 and MC23), are composed of LIW intensified patches. This confirms the findings of a fine scale resolution survey carried out in the same region (Robinson et al. 1987). We have captured an event of salinity homogenization that has ventilated the water mass properties down to 200 m connected with an anticyclonic eddy. Both AW and LIW show filaments and small spatial scale patches distributed around the jets at the border of the larger-scale eddy field.

The question of the formation and spreading of LIW in the Eastern Levantine basin has been addressed by Wust (1961) via the core method, and more recently by Ovchinnikov (1984). The latter shows that in the Northern Levantine basin the LIW formation regions are located in the central core (a few tens of kilometers in diameter) of cyclonic eddies. The spatial scales of the mixing region agree with the salinity ventilation/

homogenization process we have reported here; however the σ_t distribution inside our anticyclone is not homogeneous as in the Ovchinnikov (1984) data. As discussed previously, this could be ascribed to the different timing of the measurement or to a different process that does not involve convective density mixing. We observe the increase of salt in the upper main thermocline levels due to the intense vertical mixing between the AW and LSW layers formed during the summer, without the homogenization of density. In conclusion, this LIW renewal process seems to have a sporadic character and to happen in anticyclonic centers, in contrast to well-known cases of deep-water formation (Killworth 1979). Furthermore, because of the long time scale of movement of the eddy field here described, the speed at which this water mass spreads is expected to be very small. Moreover, because the water masses are trapped inside the persistent eddy field, the general presence of LIW in the basin, far from the source regions, could be connected to the rate of transfer of water properties between the eddies or to their movement across the basin. Recently, Holloway et al. (1986) have studied the stirring of a passive tracer field concentrated initially inside an eddy center. Their results show that the eddy can carry the tracer within it for a long time, but that there will be leaking of the tracer due to explicit diffusion or to interaction with the background flow. We believe that this mechanism of tracer or water mass transport could be active in the Levantine basin, as shown by the presence of this intense mesoscale eddy field.

7. Summary and discussion

In this paper we have presented the climatological, seasonal, and instantaneous kinematical properties of the mesoscale flow field in the southeastern Levantine basin. First, we characterized the water mass properties of the region, both climatologically and seasonally, using a 5-year-long dataset of temperature and salinity measurements. In this time and space average representation, the vertical profiles of temperature and salinity indicate the presence of different water mass layers: the LSW layer, warm and salty (see Table 2) formed during the summer season by intense evaporation and heat exchanges with the atmosphere; the AW layer, pronounced in spring, summer and autumn seasons; the LIW layer, represented by a subsurface salinity maximum and present throughout the year; and the deep layer below 700 m. Between these layers are transition layers with intermediate properties that combine aspects of the aforementioned water mass layers. The depth of these transition layers varies appreciably from season to season. The seasonal temperature changes are felt down to a depth of 170 m, which defines the depth of penetration of seasonal heat exchanges with the atmosphere. Inspection of the vertical averaged profiles indicates the possibility of double diffusive

mixing processes at the interface between the AW and LSW layers. Vertical mixing could be active between AW and LIW and between LIW and DW; in fact, the thickness of the transition layers increases appreciably during spring and autumn seasons. The cruise-by-cruise averages of the water properties show the seasonal cycle that culminates in the formation of a steep seasonal thermocline during the spring–summer seasons. The thermocline region is denoted by a moderate N^2 subsurface inflection corresponding to the layer of LIW.

The baroclinic dynamical modes and EOF of the streamfunction profiles have been calculated. The first Rossby radius of deformation is small, and the second dynamical mode is LIW layer intensified. We expect the second dynamical mode to be important for the dynamics of the mesoscale eddy field, since a large amount of its energy is contained in the second EOF. The latter is shown to account for about 20%–50% of the variance at the thermocline and deep levels.
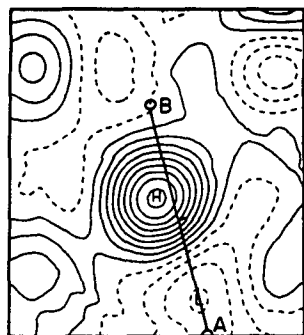
The instantaneous flow field has been objectively mapped, and time and space scales of the variability have emerged: the spatial scales are of the order of ~ 100 km (an eddy diameter), but a smaller space scale variability also seems to be relevant, even though the coarse data sampling pattern does not allow us to be conclusive. However, recent studies (Robinson et al. 1987) have shown that adequate resolution measurements can detect an energetic space scale variability of the order of 60–70 km.

A new kind of mesoscale variability, never detected before in the ocean, seems to characterize the region: isolated and persistent eddies dominate the flow field, and no westward propagation of features is evident. The time scale of the persistence varies between 6 months and a year. During this time the eddies are almost stationary in the region, undergoing noticeable changes in their strength and shape.

The velocity field peaks in the jets and current segments around the eddy centers. The velocities in the jets are of the order of 30–40 cm s^{-1} at 80 m, 20 cm s^{-1} at 230 m; and 5 cm s^{-1} at 490 m. The general circulation northeastward transport emerges from an average of the velocity field only in the northern part of the domain. The transport is contained in a meandering current within an intense eddy field.
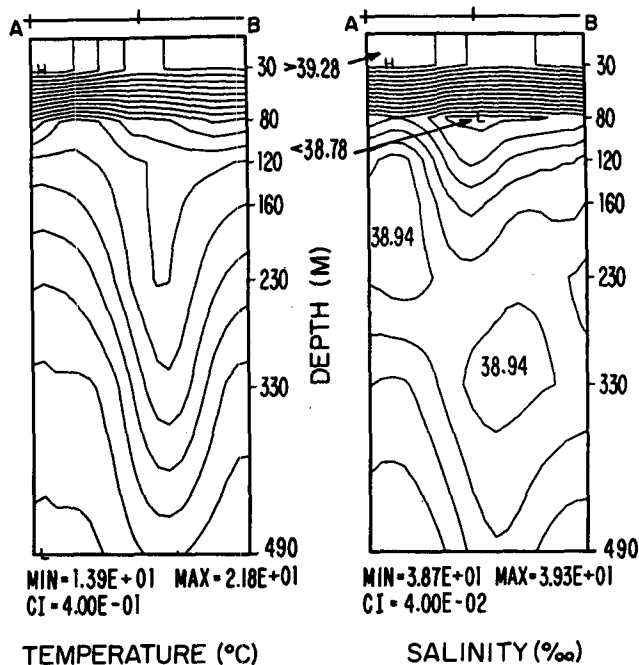
The analysis of the water mass properties of this mesoscale field shows that AW and LIW are simultaneously found in small patches and filaments around the eddy field and that any conclusion about the abundance of water mass species in the region from the average profiles could be misleading. We found that the LIW spatial distribution is highly correlated with small-scale variability in the streamfunction field. In most cases the LIW is found in patches trapped inside anticyclonic eddies. The abundance of both AW and LIW is not correlated with the seasons. Moreover, AW intrusion processes are present, and their spatial struc-

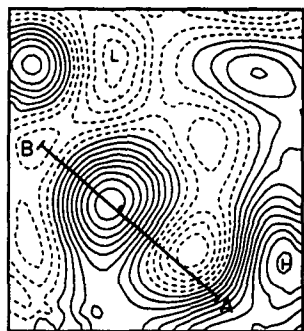a) STREAMFUNCTION MC 19

MIN=-2.05E+01 MAX=4.16E+01
CI = 5.00E+00

100 km

30 >39.28

<38.78
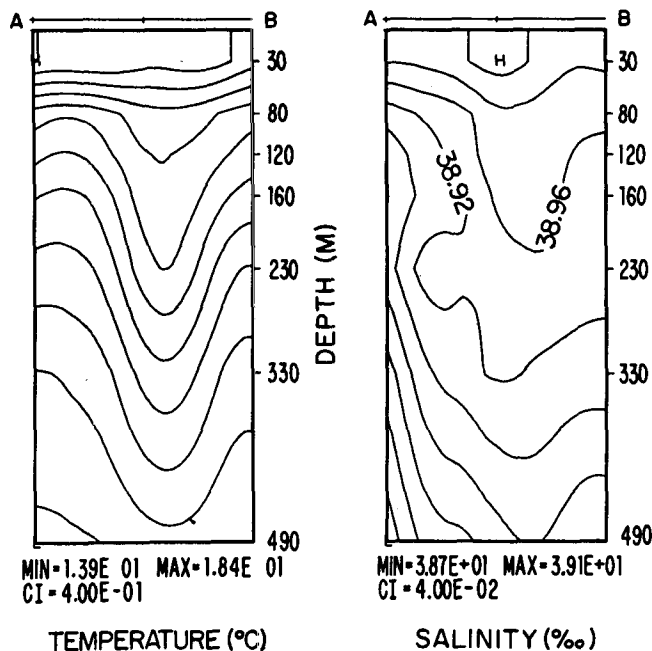
38.94

38.94

MIN=1.39E+01 MAX=2.18E+01
CI =4.00E-01

TEMPERATURE (°C)

MIN=3.87E+01 MAX=3.93E+01
CI = 4.00E-02

SALINITY (‰)

b) STREAMFUNCTION MC 20

MIN=-1.64E+01 MAX=2.56E+01
CI = 2.50E+00

100km

38.92

38.96

MIN=1.39E 01 MAX=1.84E 01
CI = 4.00E-01

TEMPERATURE (°C)

MIN=3.87E+01 MAX=3.91E+01
CI =4.00E-02

SALINITY (‰)

FIG. 23. Cross section (A-B) of temperature and salinity (a) for MC19 and (b) for MC20. Left to right: streamfunction field at 230 m with A-B cross section superimposed; isohalines as a function of depth along A-B; isotherms along A-B.

a) STREAMFUNCTION MC 25
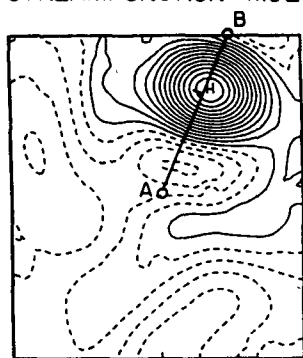
MIN = -1.21E+01 MAX = 3.24E+01
CI = 2.50E+00

100 km
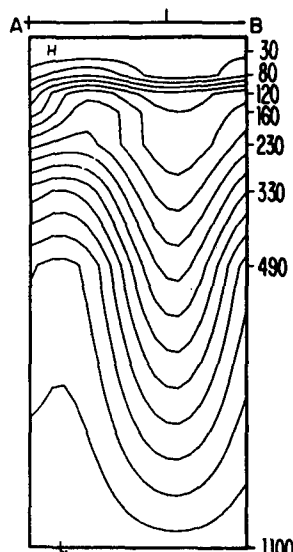
MIN = 1.36E+01 MAX = 1.70E+01
CI = 2.00E-01

TEMPERATURE (°C)

39.08
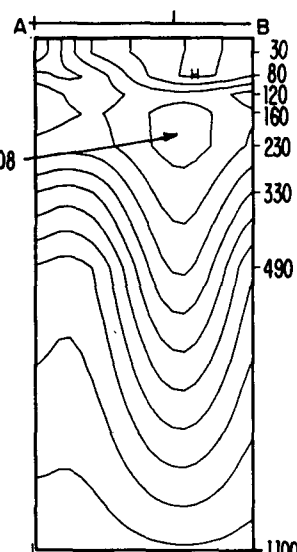
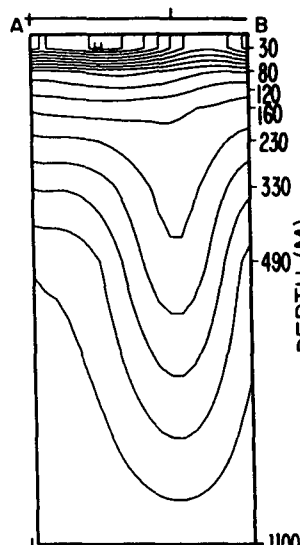MIN = 3.87E+01 MAX = 3.92E+01
CI = 4.00E-02
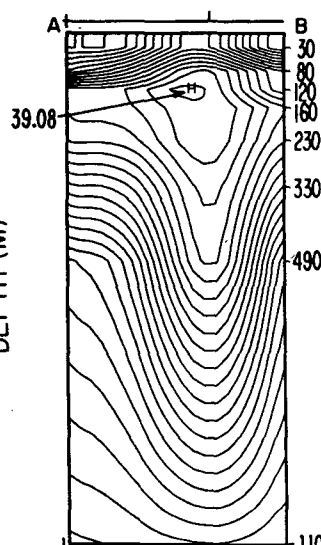
SALINITY (‰)

b) STREAMFUNCTION MC 27
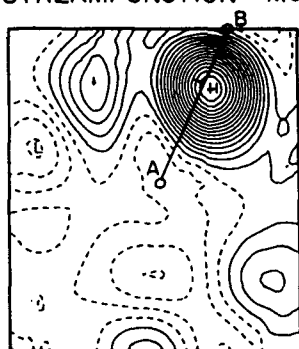
MIN = -1.03E+01 MAX = 4.01E+01
CI = 2.50E+00

100 km

MIN = 1.36E+01 MAX = 2.05E+01
CI = 4.00E-01

TEMPERATURE (°C)

39.08

MIN = 3.87E+01 MAX = 3.91E+01
CI = 2.00E-02

SALINITY (‰)

DEPTH (M)

FIG. 24. As in Fig. 23 but (a) for MC25 and (b) for MC27.

a) Temperature (°C)

b) Salinity (‰)

c) σ_t
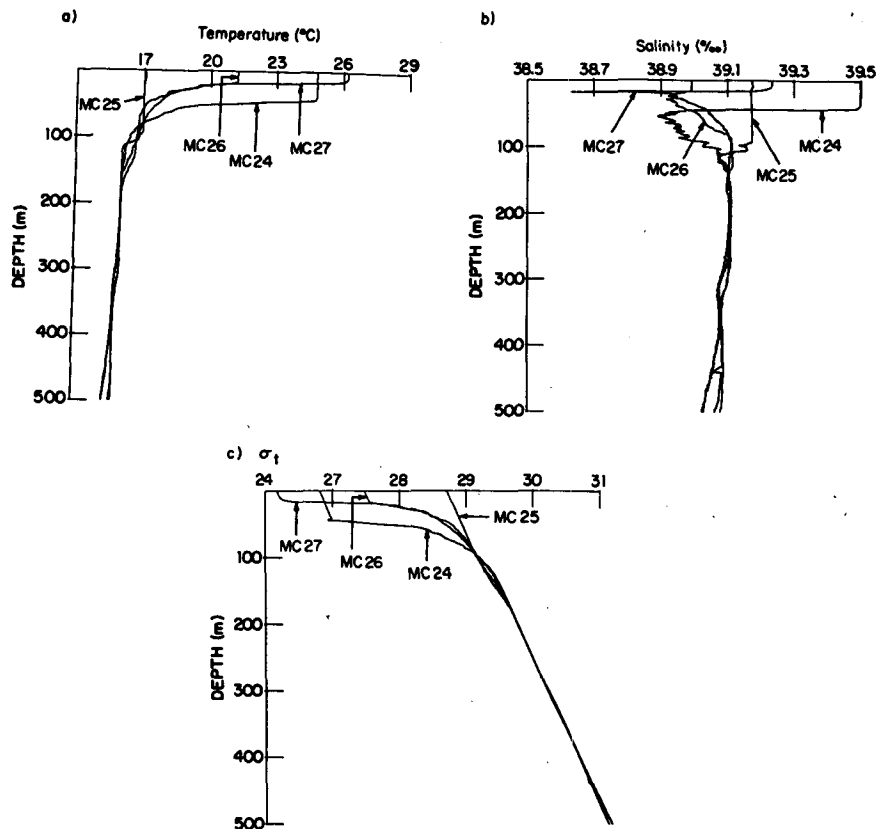
FIG. 25. Temperature (a), salenity (b) and σ_t (c) for MC24, MC25, MC26 and MC27 at station 16 (see Fig. 1b).

ture is connected to tonguelike filaments wrapping around the intense mesoscale eddy field. An event of salinity ventilation/homogenization has been captured in an anticyclonic eddy center, hinting at a localized process of renewal of upper thermocline waters.

APPENDIX

We describe here the procedure of extrapolation to 1100 m of each station profile of ψ by using the cruise by cruise NEOF profiles. To apply these eigenfunctions we have to scale the streamfunction field by the standard deviation at each level; we estimate the variance at 1100 m only from the available stations in each cruise. The normalized streamfunction anomaly $\psi''(x, y, z, t) = \psi'/\{\psi'^2\}^{1/2}$ where ψ' is defined in section 4, is taken to be represented by

$$\psi''(x_i, y_i, z_e, t) = \alpha(x_i, y_i, t)\phi_1^{NEOF}(z_e)$$
$$+ \beta(x_i, y_i, t)\phi_2^{NEOF}(z_e), \quad (A1)$$

where i indicates the station, x_i, y_i its geographical position, and z_e the level. The combination of ϕ_1^{NEOF} and ϕ_2^{NEOF} captures at all the levels more than 90% of the variance, so that we can disregard any higher mode contribution in (A1). The third and fourth ϕ_n^{NEOF} are usually in the noise level of the matrix inversion calculation (because of the small eigenvalue to which they correspond), and we do not use them. To evaluate α and β we use a simple least squares fit on the ϕ_n^{NEOF} amplitudes at each station and for each level available at that particular station. We then rescale by the standard deviation at each level to obtain ψ'. The residual variance of the least squares projection is of the order

of a few percent for the first seven levels, where we have all the stations. In other words, using only two NEOF we can reproduce the available data to within a few percent. We think that this vertical extrapolation procedure is more valuable than any horizontal extrapolation technique we could have tried via objective analysis.

REFERENCES

Anati, D. A., 1977: Topics in the physics of the Mediterranean Sea. Ph.D. Thesis, Weizmann Institute of Science, Rehovot, Israel, 43 pp.

Carter, D. B., 1956: The water balance of the Mediterranean and Black seas. *Publ. Climatol.,* Drexel Institute of Technology, Lab. Climatol., Centeron, New Jersey **9,** 123–175.

Carter, E. F., and A. R. Robinson, 1987: Analysis models for the estimation of oceanic fields. *J Atmos. Oceanic Technol.,* **4**(1), 49–74.

De Mey, P., and A. R. Robinson, 1987: Simulation and assimilation of satellite altimeter data on the oceanic mesoscale. *J. Phys. Oceanogr.,* in press.

Emery, W. J., and J. S. Dewar, 1982: Mean temperature–salinity, salinity–depth, and temperature–depth curves for the North Atlantic and the North Pacific. *Progress in Oceanography* Vol. 11, Pergamon, 219–305.

——, W. G. Lee and L. Magaard, 1984: Geographic and seasonal distribution of Brunt–Väisälä frequency and Rosby radii in the North Pacific and the North Atlantic. *J. Phys. Oceanogr.,* **14**(2), 294–317.

Feliks, Y., and S. Itzikowitz, 1987: Movement and geographical distribution of anticyclonic eddies in the eastern Levantine basin. *Deep-Sea Res.,* **34**(9A), 1499–1508.

Fofonoff, N. P., and R. C. Millard, Jr., 1983: Algorithms for computation of fundamental properties of seawater. UNESCO Tech. Pap. in Mar. Sci. No. 44, 53 pp.

——, S. P. Hayes and R. C. Millard, Jr., 1974: WHOI/Brown CTD microprofiler: Methods of calibration and data handling. Woods Hole Oceanographic Institution, Tech. Rep. WHOI 74–89, 64 pp.

Hecht, A., 1986: The hydrology and the water masses of the Eastern Mediterranean Sea. *Proceedings of UNESCO/IOC workshop on Physical Oceanography of the Eastern Mediterranean,* A. R. Robinson and P. Malanotte-Rizzoli, Eds., Middle East Technical University, Erdemli, Turkey.

——, Z. Rosentroub and Y. Bishop, 1985: Temporal and spacial variations of heat storage in the Eastern Mediterranean. *Israel J. Earth Sci.,* **34**(2/3), 51–64.

Holloway, G., S. C. Riser and D. Ramsden, 1986: Tracer anomaly evolution in the flow field of an isolated eddy. *Dyn. Atmos. Oceans,* **10,** 165–184.

Hua, B. L., J. C. McWilliams and W. B. Owens, 1986: An objective analysis of the POLYMODE local dynamics experiment. Part II: Streamfunction and potential vorticity fields during the intensive period. *J. Phys. Oceanogr.,* **16**(3), 506–522.

Killworth, P. D., 1979: On "Chimney" formations in the ocean. *J. Phys. Oceanogr.,* **9**(5), 531–554.

Kutzbach, J. E., 1967: Empirical eigenvectors of sea level pressure, surface temperature and precipitation complexes over North America. *J. Appl. Meteor.,* **6,** 791–802.

Lacombe, H., and P. Tchernia, 1960: Quelques traits generaux de l'hydrologie Mediterraneenne d'pres diverses campagnes hydrologiques recentes en Mediterranee dans la poche Atlantique et dans le detroit de Gibraltar. *Cah. Oceanogr.,* **12**(8), 527–547.

——, and ——, 1972: Caractere hydrologique et circulation des eaux en Mediterranee. *The Mediterranean Sea: A Natural Sedimentation Laboratory.* D. J. Stanley, Ed., Dowden, Hutchinson & Ross, 25–36.

Lau, N-G., 1981: A diagnostic study of recurrent meteorological

anomalies appearing in a 15-year simulation with a GFDL general circulation model. *Mon. Wea. Rev.,* **109,** 2287–2311.

Lorenz, E., 1956: Empirical orthogonal functions and statistical weather prediction. M.I.T. Meteorology Department, Scientific Rep. No. 1.

McWilliams, J. C., W. B. Owens and B. L. Hua, 1986: An objective analysis of the POLYMODE local dynamics experiment. Part I: General formalism and statistical model selection. *J. Phys. Oceanogr.,* **16,** 483–504.

Mooers, C. N. K., and A. R. Robinson, 1984: Turbulent jets and eddies in the California current and inferred cross-shore transports. *Science,* **223,** 51–53.

Morcos, A. S., 1972: Sources of Mediterranean intermediate water in the Levantine Sea. *Stud. Phys. Oceanogr.,* Vol. 2. A. L. Gordon, Ed., Gordon & Breach, 185–206.

Morel, A., 1971: Caracteres hydrologiques des eaux echangees entre le bassin Oriental et le bassin Occidental de la Mediterranee. *Cah. Ocean.,* **23**(4), 329–342.

Moskalenko, L. V., and I. M. Ovchinnikov, 1965: The water masses of the Mediterranean Sea. *Basic Features of the Geological Structure, Hydrological Regime and Biology of the Mediterranean.* L. M. Fomin, Ed., translation of the Institute for Modern Languages for the U.S. Naval Oceanogr. Office, 202–218a.

Ovchinnikov, I. M., 1966: Circulation in the surface and intermediate layers of the Mediterranean. *Oceanology,* **6,** 49–59.

——, 1984: The formation of intermediate water in the Mediterranean. *Oceanology,* **24,** 168–173.

Ozsoy, E., H. A. Latif and U. Unluata, 1981: On the formation of Levantine Intermediate water. *Rapp. Comm. Int. Mer Medit.,* **27**(6), 51–65.

Ozturgut, E., 1976: The sources and spreading of the Levantine Intermediate Water in the Eastern Mediterranean. SACLANT-CEN-SM-92, 45 pp.

Pedlosky, J., 1979: *Geophysical Fluid Dynamics,* Springer-Verlag, 624 pp.

Pinardi, N., and A. R. Robinson, 1987: Dynamics of deep thermocline jets in the POLYMODE region. *J. Phys. Oceanogr.,* **17**(8), 1163–1188.

Robinson, A. R., J. A. Carton, N. Pinardi and C. N. K. Mooers, 1986: Dynamical forecasting and dynamical interpolation: An experiment in the California current. *J. Phys. Oceanogr.,* **16,** 1561–1579.

——, A. Hecht, N. Pinardi, Y. Bishop, W. G. Leslie, Z. Rosentroub, A. J. Mariano and S. Brenner, 1987: Small synoptic/mesoscale eddies: The energetic variability of the Eastern Levantine Basin. *Nature,* **327**(6118), 131–134.

Smith, J. A., C. N. K. Mooers and A. R. Robinson, 1985: Estimation of quasi-geostrophic model amplitudes from XBT/CTD survey data. *J. Atmos. Oceanic Technol.,* **2**(4), 491–507.

Stommel, H., 1972: Deep wintertime convection in the western Mediterranean Sea. *Stud. in Phys. Oceanogr.,* Vol. 2. A. L. Gordon, Ed., Gordon & Breach, 207–218.

Taft, B. A., E. J. Lindstrom, C. C. Ebbesmeyer, C. Y. Shen and J. C. McWilliams, 1983: Water mass structure during POLYMODE local dynamics experiment. *J. Phys. Oceanogr.,* **16,** 403–426.

Trenberth, K. E., 1983: What are the seasons? *Bull. Amer. Meteor. Soc.,* **64**(11), 1276–1282.

Turner, J. S., 1974: Double-diffusive phenomena. *Ann. Rev. Fluid Mech.,* **6,** 37–56.

——, 1978: Double-diffusive intrusions into a density gradient. *J. Geophys. Res.,* **83**(C6), 2887–2901.

UNESCO, 1984: Physical oceanography of the Eastern Mediterranean: An overview and research plan. Rep. in Marine Sciences No. 30, Rep. of Workshop from Lerici, La Spezia, Italy.

Wust, G., 1960: Die tiefenzirkulation des mitlandischen meeres in den kerenshichtendes zwischen und des tieferwassers. *Deutsch. Hydrogr.,* A13(3), 105–131.

——, 1961: On the vertical circulation of the Mediterranean Sea. *J. Geophys. Res.,* **66**(10), 3261–3271.